Surface & Coatings Technology 512 (2025) 132386

Contents lists available at ScienceDirect

Surface & Coatings Technology

journal homepage: www.elsevier.com/locate/surfcoat

HVOF deposition of TiC-based hardmetal coatings with High-Entropy Alloy (HEA) matrix

Giovanni Bolelli [a,*], Maria Francesca Bonilauri [a], Luca Bortolotti [a], Alessia Bruera [a], Margherita Cescon [a], Lorenzo Ferrari [a], Magdalena Lassinantti Gualtieri [a], Luca Lusvarghi [a], Stefania Morelli [a], Milena Pazzi [a], Alvise Bianchin [b], Enrico Forlin [b], Giulia Gigante [c], Edoardo Rossi [c], Marco Sebastiani [c]

[a] Dipartimento di Ingegneria "Enzo Ferrari", Università di Modena e Reggio Emilia, Via Pietro Vivarelli 10/1, 41125 Modena, MO, Italy
[b] MBN Nanomaterialia S.r.l., Carbonera, TV, Italy
[c] Dipartimento Di Ingegneria Civile, Informatica e Delle Tecnologie Aeronautiche, Università di Roma Tre, Roma, Italy

ARTICLE INFO

Keywords:
High-entropy alloy
TiC-based hardmetals
High velocity oxy-fuel (HVOF)
Sliding wear
Abrasion
Nanoindentation

ABSTRACT

To provide wear-resistant substitutes to conventional WC-Co-based coatings for industrial applications, this work investigates the high-velocity oxygen fuel (HVOF) deposition of TiC-based hardmetal coatings with high-entropy alloy (HEA) matrices. The microstructural features, phase composition, and mechanical properties of four HEA matrix formulations, namely CrMnFeCoNi ("Cantor" alloy), $Cr_{20}Mn_{25}Fe_{40}Ni_{15}$, $Al_{14}(Cr_{20}Mn_{25}Fe_{40}Ni_{15})_{86}$, and $Al_{0.5}CrCuFeNi_2$, coupled with 60 vol% TiC were evaluated. The HEA matrices contained a homogeneous distribution of TiC particles, according to microstructural examination, and the compositions incorporating Al had lower degrees of oxidation and decarburization. While the Cantor+60TiC and $Al_{0.5}CrCuFeNi_2$ + 60TiC coatings showed higher hardness and critical loads in mechanical tests, the $Al_{14}(Cr_{20}Mn_{25}Fe_{40}Ni_{15})_{86}$ + 60TiC coatings showed more brittle behaviour. Discrete mechanical phases were identified by nanoindentation mapping and Gaussian Mixture Model analysis, and their hardness values were correlated with microstructural features. These findings underscore the potential of HEA-TiC hardmetal systems as wear-resistant coatings, particularly the $Al_{0.5}CrCuFeNi_2$ + 60TiC composition, which demonstrated superior oxidation resistance and mechanical robustness compared to the other formulations, and is free of cobalt. The insights gained will also serve as a foundation for AI-driven optimization of HEA compositions for targeted applications.

1. Introduction

High-entropy alloys (HEAs) are defined, from a compositional point of view, as equiatomic or near-equiatomic alloys of 5 or more elements, and, from a thermodynamic point of view, as being characterized by an entropy of mixing $\Delta S_{mix} > 1.61 \cdot R$, where R is the ideal gas constant [1,2]. It is generally believed that this large entropy of mixing results in the thermodynamic stabilization of simple solid solutions with a highly symmetric lattice: face-centred cubic (FCC), body-centred cubic (BCC), or, more rarely and mostly with refractory elements-based systems, hexagonal close-packed (HCP) [2]. High symmetry indeed means that there are many equivalent lattice positions: when each position can be randomly occupied by many possible elements, the configurational entropy of the system, which depends on the number of equivalent configurations, becomes very large. Therefore, it is assumed that, driven by the entropy term, the Gibbs' free energy of a random solid solution $G^{SS} = H^{SS} - T \cdot S^{SS}$ is lower than that of a multi-phase system made of several ordered intermetallic phases, $G^{IM} = H^{IM} - T \cdot S^{IM}$. This is especially true if the enthalpy of mixing of the elements in the random solid solution H^{SS} is close to zero, that is, if the chosen elements respect the classical Hume-Rothery rules of solid solubility [2–7]. Thus, systems that constitute a proper HEA consist of only one solid solution phase. It should be noted that these simplified assumptions are not always correct [1]. As reviewed in detail in [2], the actual values of the various enthalpy and entropy terms listed above can deviate substantially from the ideal ones. Thus, it can be rather complex to predict the actual phase composition of a HEA system. For example, elements with different atomic radii seldom give rise to truly "ideal" solid solutions with entirely

---

* Corresponding author.
E-mail address: giovanni.bolelli@unimore.it (G. Bolelli).

https://doi.org/10.1016/j.surfcoat.2025.132386
Received 18 January 2025; Received in revised form 8 June 2025; Accepted 9 June 2025
Available online 10 June 2025

random distribution and a near-zero enthalpy of mixing. Conversely, the entropy of an intermetallic phase in a multi-component system might be itself relatively high. Thus, depending on their chemical composition, some multi-element mixtures develop more than one phase, ranging from biphasic systems made of two solid solutions (e.g., FCC + BCC) to more complex systems, which have become increasingly common as the research veers toward non-equiatomic mixtures.

The above considerations mean that the “high entropy” concept might not be appropriate in all cases; therefore, other terms have also been introduced to designate these alloys: multi-principal element alloys, complex concentrated alloys, multi-component alloys, etc. [7]. Sometimes, the term HEA might be reserved for equiatomic systems, and other terms can be used for non-equiatomic ones. However, since there is still no consensus in the field, the term “high-entropy alloy” (HEA) will be used hereafter in this paper to refer to all the equiatomic and non-equiatomic multielement systems considered here.

Whether the concept of phase stabilization through configurational entropy is rigorously true or not, these alloys do have very interesting mechanical and functional properties.

Generally, HEAs are often shown to be in the upper right corner of an Ashby map of fracture toughness versus yield strength [8]. More specifically, FCC HEAs based on 3d transition metals usually exhibit relatively low hardness and yield strength, comparable to common FCC alloys like austenitic stainless steels, but possess excellent work-hardening ability, better than conventional FCC metals [1,2,9,10]. This could be desirable in various applications, including tribological ones because it means that toughness in the bulk of the material is coupled to the ability to develop high hardness “on demand”, under contact conditions. The references cited above provide various mechanisms to explain this exceptional strain-hardening behaviour. One of them is the propensity of Co-containing HEAs toward twinning because of their low stacking-fault energy (SFE). In fact, the formation of twins during plastic deformation impedes the movement of dislocations [1,9,10].

BCC HEAs are usually harder but also more brittle [9]. Strengthening can also be achieved by adding secondary elements to a HEA to induce the formation of controlled amounts of second phases, like BCC or intermetallics, in a mainly FCC system. As a result, higher hardness and yield strength are obtained at the expense of toughness and ductility [11].

Due to these desirable features, the manufacture of protective coatings is one of the possible applications envisaged for HEAs [2,6,12,13]. In fact, the deposition of HEA layers has been pursued in the literature using all the main categories of physical coating deposition processes: cladding (e.g., laser cladding [14]), thermal spraying [15] and physical vapour deposition [16].

In the field of thermal spraying, in particular, Meghwal et al. [15] provided a comprehensive review of the efforts made so far to deposit HEA coatings. The review shows that experiments have already been carried out with some of the most common HEA systems based on 3d transition metals with possible additions of elements such as Al, Si, Mo, Nb, etc. However, the use of HEAs as potential matrices for hardmetal coatings, where a “hardmetal” is defined as a metal-ceramic composite that contains between 60 vol% and 90 vol% of the hard ceramic phase [17], is an almost unexplored area in the field of thermal spraying. The only report of an actual hardmetal coating was recently provided by Xiao et al., who processed a powder consisting of a HEA matrix ($Al_{1.8}CuFeCrNi_2$) with 50 wt% TiC by the High Velocity Air-Fuel (HVAF) technique [18]. The sliding wear rates measured by ball-on-disc tests against a ZrO_2 ball at 10 N and 25 N normal load were 6.3×10^{-5} $mm^3/(N\bullet m)$ and 4.2×10^{-5} $mm^3/(N\bullet m)$, respectively. These results can be regarded as not particularly impressive: in comparison, the ball-on-disc sliding wear rates that we measured in our previous work on TiC-based coatings with simpler Ni- or Fe-based matrices using Al_2O_3 as a counterpart were approximately between 2×10^{-7} $mm^3/(N\bullet m)$ and 2×10^{-6} $mm^3/(N\bullet m)$ [19]. Thus, judging from this single result, more research is needed to establish whether HEA matrices can provide actual improvements over conventional ones in hardmetal coatings. Another paper reported on the High Velocity Oxygen-Fuel (HVOF) processing of blends of an AlCoCrFeNi powder with up to 50 wt% of a WC-10wt.%Co hardmetal powder [20]. The coatings covered in this study would probably be more suitably called metal-matrix composites than hardmetals. The cited study [20] focused on solid particle erosion and showed that the addition of the hardmetal improved the erosion resistance of the AlCoCrFeNi-based coatings, but the performance of the composites was not compared to any reference material. Therefore, it is not possible to assess whether the HEA matrix brought about specific benefits.

To the contrary, reports on carbide-reinforced HEA coatings obtained by cladding technologies are much more frequent. It is not the purpose of this paper to provide a complete review of the literature, but looking at a sub-set of representative recent papers [21–27], it is inferred that:

- The more frequently employed hard phase is still WC, but sometimes also NbC or TiC are used.
- The specific wear rates measured under ball-on-disc sliding conditions against counterparts made of Al_2O_3, Si_3N_4 or hardmetal attained minima roughly comprised in the range of 2×10^{-6} $mm^3/(N\bullet m)$ to 5×10^{-6} $mm^3/(N\bullet m)$ when the feedstock material contained 30 to 60 wt% of WC, although in one case, specific wear rates of the order of 10^{-7} $mm^3/(N\bullet m)$ were found.

Again, these results do not seem much better than what has already been achieved with more conventional metal matrices. Thus, there is still ample room to investigate the thermal spray deposition of hardmetal coatings with HEA matrices.

Another shortcoming of the current state of research on thermal spray HEAs is the fact that most of the reports so far [15] involve Co-containing alloys. However, cobalt is a critical raw material (for example, it has been classified as such by the European Union [28]) and a recognized carcinogen [29–34], representing a potential barrier for future widespread application of such coatings.

Therefore, the present research aims to study the deposition of hardmetal coatings with HEA matrices, including Co-free ones, and a hard phase such as TiC, which would allow the replacement of another critical raw material, namely tungsten [28]. We chose to use the HVOF process, which is one of the main techniques used to deposit wear- and corrosion-resistant coatings [35–40]. The compositions of the HEA matrices were selected from the literature to cover a range of possibilities going from Co-containing to Co-free alloys and from single-phase FCC to single-phase BCC and two-phase systems. Details of the selection of the HEA matrix compositions for this work are given in Section 2.1.

2. Materials and methods

2.1. Compositions’ choice and powder manufacturing

Four different HEA compositions were chosen as matrix materials. The compositions given hereafter are all expressed in atoms unless stated otherwise:

- The “Cantor” alloy, i.e., an equiatomic Cr-Mn-Fe-Co-Ni mixture. This material still contains cobalt, but it was selected because it has been the first and is still one of the most studied and better-known HEA systems [7]. Thus, it can serve as a good reference for other systems with Co-free HEA matrices for which fewer literature works exist. The “Cantor” alloy is characterized by an FCC matrix with high ductility and good mechanical strength at the same time.
- The $Al_x(Cr_{20}Mn_{25}Fe_{40}Ni_{15})_{100-x}$ system studied in [41], which is free from Co and whose phase composition and mechanical properties

can be tuned via the Al content. Specifically, the extremes x = 0 and x = 14 were chosen. According to [41], these compositions correspond, respectively, to a mostly FCC system with a compressive yield strength of around 200 MPa and to a fully BCC system (a BCC random solid solution plus an ordered B2 BCC phase) with yield strength slightly above 900 MPa. In the cited reference, the phase change was ascribed to the decrease in valence electron concentration (VEC) with increasing amounts of Al, starting from a non-equiatomic Cr-Mn-Fe-Ni system, which is already on the verge of developing the BCC phase [41]. In fact, the VEC is a well-known criterion for assessing the tendency of a HEA to form an FCC phase (VEC > 8), a BCC (VEC < 6.87) phase, or a mixture of both (6.87 < VEC < 8) [5]. In addition, Al- and Fe-rich compositions in the Al-Cr-Mn-Fe-Ni system also exhibit a low value (~10) of the parameter $\varphi = (S_C - |\Delta H_{mix}|/T_m)/|S_E|$, where S_C = configurational entropy of mixing, S_E = excess entropy of mixing (negative and usually decreasing in absolute value with increasing temperature), ΔH_{mix} = mixing enthalpy, T_m = melting temperature [42]. Usually, systems with $\varphi < 20$ develop multiphase structures whilst $\varphi > 20$ implies effective entropic stabilization of a single-phase system [42]. Choosing the two extremes x = 0 and x = 14 allows to study the effects of varying the phase composition of the matrix.
- The $Al_{0.5}CrCuFeNi_2$ studied in [43], which is also Co-free and accepts a rather substantial amount of Al (approximately 9 at.%) while still developing, under equilibrium conditions, a prevailing FCC structure with high ductility: approximately 350 MPa yield strength, 500 MPa ultimate tensile strength, and 16 % elongation in as-cast condition. Due to the presence of excess Ni compared to an equiatomic mixture, indeed, this composition has VEC > 8 [42] and φ ~20. This allows further exploration of the range of possible combinations when compared with the $Al_x(Cr_{20}Mn_{25}Fe_{40}Ni_{15})_{100-x}$ system, where a high Al content is instead coupled with a BCC phase.

All these compositions were combined with 60 vol% TiC as the hard phase. Previous studies on TiC-based hardmetal systems with simpler matrices (Ni-20wt.%Cr, Fe-Cr-Al, etc.) showed this amount of hard phase to provide a proper balance between hardness and toughness, whereas higher hard phase contents usually resulted in excessive brittleness [19,44,45]. The same happened when NbC was used instead of TiC as a hard phase [46].

Thus, the following 4 hardmetal systems were considered in this work:

- CrMnFeCoNi + 60 vol% (47.8 wt%) TiC, hereafter labelled as "Cantor+60TiC"
- $Cr_{20}Mn_{25}Fe_{40}Ni_{15}$ + 60 vol% (48.6 wt%) TiC, hereafter labelled as "Al_0(CrMnFeNi) + 60TiC"
- $Al_{14}(Cr_{20}Mn_{25}Fe_{40}Ni_{15})_{86}$ + 60 vol% (51.9 wt%) TiC, hereafter labelled as "Al_{14}(CrMnFeNi) + 60TiC"
- $Al_{0.5}CrCuFeNi_2$ + 60 vol% (49.0 wt%) TiC, hereafter labelled as "AlCrCuFeNi+60TiC".

Feedstock powders with the respective compositions were obtained by MBN Nanomaterialia (Vascon-TV, Italy) via a proprietary industrial high-energy ball milling (HEBM) process. Mixtures of elemental powders of the matrix elements, Ti, and graphite were weighed in the proper amounts to achieve the compositions listed above, considering the density and atomic mass of the individual constituents to compute the needed mass of each element. HEBM is a particularly viable choice for the manufacture of HEAs due to its productivity and versatility, as reviewed by Kumar et al. [13]. The solid-state synthesis of TiC was achieved in situ during the HEBM process, as the Gibbs free energy of formation of TiC is more negative than that of any of the carbides of the matrix elements. This ensured a fine and uniform distribution of TiC in the matrix and a firm interface bonding. The HEBM powders were air classified and sieved to a nominal size distribution of −45 + 15 μm, suitable for thermal spray processing.

Table 1
HVOF deposition parameters for all powders.

Parameter setting	Run1	Run2	Run3
O_2 pressure (psi/MPa)	170/1.20		
O_2 flow rate (SLPM)	201	214	228
H_2 pressure (psi/MPa)	140/0.98		
H_2 flow rate (SLPM)	574	635	656
Air pressure (psi/MPa)	100/0.7		
Air flow rate (SLPM)	274		
Stoichiometric ratio	0.9	0.86	0.87
Powder feed rate (g/min)	20		
Stand-off distance (mm)	250		
Torch-substrate speed (mm/s)	750		
Pitch distance (mm)	5		
N° of passes per cycle	3		
N° of deposition cycles	13		
N° of preheating cycles	1		
Pause between cycles (s)	20		

2.2. Coatings deposition

All coatings were deposited by HVOF spraying onto AISI304 stainless steel plates of 60 × 25 × 3 mm size, which were grit-blasted using brown alumina with a median particle size (d_{50}) of ~300 μm with handheld blasting equipment operated at a pressure of 5.5 bar. The plates were then cleaned in an ultrasonic bath with acetone to remove loose grit residuals and contaminations, dried with compressed air, and stored in a stove at 60 °C to avoid humidity build-up prior to deposition.

The deposition was carried out using a Diamond Jet 2600 HVOF system (Oerlikon Metco US Inc., Westbury, NY, USA) equipped with a DJ8W torch featuring hybrid water+air cooling and a gravimetric 9MPE-DJ powder feeder based on a pressurized fluidized-bed system.

The torch was mounted on an X-Y translation system, whilst the plates were loaded onto a rotating mandrel. In all cases, the rotation speed of the mandrel and the horizontal traverse speed of the torch were set to achieve a relative torch-to-substrate velocity of 750 mm/s and a pitch distance of 5 mm. The torch was traversed back and forth in front of the substrates in three consecutive passes for each deposition cycle, and a total of 13 consecutive cycles were performed with a pause of 20 s between them to allow for substrate cooling. Fixed compressed air jets were directed at the plates to limit the deposition temperature and avoid accumulation of overspray between passes.

Prior to deposition, one 3-pass cycle was performed without powder feed and without cooling air to preheat the substrates. The powder feeder was then switched on and deposition started as soon as the feed rate stabilized to within ±4 g/min of the desired value, which usually took around or slightly <1 min.

During deposition, the system's surface temperature was monitored with an infrared pyrometer (OPTRIS CTLaser, Luchsinger srl, Curno, Italy), which was aimed to a position away from the torch scan track to avoid artefacts due to the spray jet's emission.

For all powders, three depositions were carried out using three different parameter sets, designated as "Run 1" to "Run 3". These sets had increasingly high H_2 and O_2 flow rates, as detailed in Table 1, while all other parameters were kept constant.

The deposition efficiency was measured by weighing three plates before and after deposition for each run using an electronic balance with ±0.01 g accuracy. The mass gain of the sample was divided over the overall mass of powder sprayed toward each plate, which was computed from the powder feed rate, the plate size, and the torch/substrate kinematics (relative speed, pitch distance, number of passes/cycle, and number of deposition cycles).

In addition, a standard WC-CoCr coating was also deposited on the same substrates using a commercially available powder (Woka 3652, Oerlikon Metco WOKA GmbH, Barchfeld, Germany) and the process conditions previously described in [47]. This coating was used as a comparison term for micromechanical (Section 2.3.2) and wear (Section 2.3.3) tests.

2.3. *Characterization of powders and coatings*

2.3.1. *Microstructure and phase composition*

The cross-sectional microstructure of the powders and coatings was checked by scanning electron microscopy (SEM: Nova NanoSEM 450, FEI – Thermo Fischer Scientific, Eindhoven, NL), with qualitative and quantitative compositional analysis by Energy-Dispersive X-ray (EDX) spectroscopy (Quantax200 EDX microanalysis system with XFlash6|10 detector, Bruker Nano GmbH, Berlin, Germany). The powders were mounted in a two-component epoxy resin cured at room temperature. The coated plates were cut with a resin-bound Al_2O_3 abrasive disc and hot-mounted in phenol-based resin with fillers using a press. Subsequently, the powders and coatings were ground with SiC-based abrasive papers of P400 to P4000 size and sequentially polished using a polycrystalline diamond suspension (3 μm average particle size) and colloidal silica. The samples were then ultrasonically cleaned with acetone, dried with compressed air, and mounted on standard aluminium specimen stubs with conductive adhesive tapes. No metallization was applied to the sample surfaces prior to the observation, as the powder-loaded resin was electrically conductive, whilst the phenol-based resin had sufficient intrinsic electrical conductivity.

The quantitative chemical composition of the powders and coatings was measured by acquiring three EDX spectra on 400× views of the cross-sections of powders and coatings operating at 15 kV electron beam acceleration voltage with a live time of 60 s. Quantification was carried out using the Esprit 2.1 software with the φ-ρ-Z method. Carbon and oxygen were quantified by EDX in the coatings, but they were excluded from the quantification for the powders, since the large-area EDX scans, in this case, encompassed both particles and the epoxy resin, which contains C and O as its main constituents.

To quantify oxygen, nitrogen, and carbon in the powders, elemental analyses were performed using the oxygen combustion method (for carbon: TCH600 instrument, LECO Corporation, St. Joseph, MI, USA) and the inert gas fusion technique (for oxygen and nitrogen: CS230 instrument, LECO Corporation), according to the procedure previously described in [45]. The EDX results were then renormalized to 100 by including the results of the elemental analysis.

Porosity measurements were performed by image analysis on eight micrographs acquired in backscattered electron mode at 3000× using a Matlab (R2024a – The MathWorks Inc., USA) procedure. Thickness was measured by image analysis on 400× micrographs using the ImageJ software (NIH, Bethesda, MA, USA).

The phase composition of the powders and coatings was assessed by X-ray diffraction (XRD: X'Pert PRO and Empyrean, Malvern Panalytical, Almelo, NL), using Cu-Kα radiation from a tube operated at 40 kV and 40 mA, in the $20^\circ < 2\theta < 85^\circ$ range. The coating surfaces for the XRD measurements were ground using diamond-based abrasive papers (P120, P400, P600) and pads with polycrystalline diamond suspensions (9 μm and 3 μm average size), then polished using a cloth again with a 3 μm polycrystalline diamond suspension.

Crystallographic phases were identified using the X'Pert HighScore Plus software (version 5.1, Malvern Panalytical) [48] equipped with the ICDD PDF-4 database. Rietveld refinements for semiquantitative phase analyses were performed using the GSAS-EXPGUI package [49,50]. Structure models were obtained from the Crystallography Open Database (COD) [51]. The peak profiles were fitted with a pseudo-Voigt function ("type 2" profile shape model in GSAS) [49]. The unit cell parameters and the scale factor for each constituting phase were refined, along with the background (shifted Chebyshev function with nine terms) and the zero shift.

Table 2
High-speed nanoindentation mapping parameters.

Sample	Target load (mN)	X size (μm)	Y size (μm)	Number of indents	Average depth (nm)
Cantor+60TiC	2.3	200	280	56,000	83
Al_0(CrMnFeNi) + 60TiC	3	120	120	14,400	96
Al_{14}(CrMnFeNi) + 60TiC	3.5	242	273	65,502	114
AlCuCrFeNi+60TiC	3	150	150	22,500	95

2.3.2. *Micromechanical testing*

Cross-sections polished as described in Section 2.3.1 were also employed to measure the coatings' microhardness by depth-sensing microindentation (Micro-Combi Tester, Anton Paar Tritec, Corcelles, CH). A Vickers indenter was employed, with an applied load of 3 N, a loading and unloading time of 30 s each, and a hold of 15 s at maximum load. The curves were analysed using the Oliver-Pharr method, following ISO 14577. Twenty indents were made in each sample, and the results were expressed as mean ± standard deviation.

High-speed nanoindentation mapping [52] was performed across the thickness of the coatings, from the substrate to the outer surface, to map the mechanical properties and local heterogeneity distributions. Based on the standard Oliver-Pharr procedure [53], this method integrates advances in hardware, electronics, and data management, enabling rapid execution of tests (1 to 5 s per load-unload cycle). A G200 nanoindenter (KLA Corporation, Oak Ridge, TN, USA) with a standard Berkovich tip was used for high-speed grid indentations. The lateral extension and the number of indents per sample, adjusted based on the time-resolution trade-off, are presented in Table 1. The indentation spacing followed the criterion of 10 times the indentation depth, preventing the overlap of the plastic zones, as recommended by Vignesh et al. and Phani et al. [54,55]. Prior to testing, grid continuous stiffness measurements were performed on each sample to calibrate its load-displacement response. This served as the selection means for the target load in the load-controlled high-speed nanoindentation mapping (values are reported in Table 2).

The machine compliance and indenter area function were calibrated using the same high-speed methodology used for the actual maps.

After the experiments, the hardness values taken from the nanoindentation maps were analysed using the Gaussian Mixture Model (GMM) algorithm [56], with the final objective of deciphering the mechanical phase composition of the coatings. This approach assumes a normal distribution of the components. It allows for deconvolution of the dataset via an expectation-maximization protocol.

Surfaces ground and polished in the same way as described for the XRD analysis in Section 2.3.1 were used for scratch testing. Scratch tests (Micro-Combi Tester) were performed using a conical diamond indenter (120° opening) with a spherical tip (100 μm tip radius). On each surface, six tracks were performed with a linearly increasing load from 0.02 mN to 30 N, over a length of 6 mm with a speed of 6 mm/min. The tracks were inspected by optical microscopy at 200× magnifications to identify the failure modes and the associated critical loads for their onset. Instrumental recordings of acoustic emission, tangential force (and friction coefficient), and total and residual depth of penetration (obtained through pre- and post-scans performed with the same tip at a 0.02 N load) were also acquired to assist in the critical loads' identification.

2.3.3. *Wear testing*

Ball-on-disc sliding wear tests were carried out in unidirectional rotation mode according to ASTM G99, using the same polished samples employed for XRD analysis and scratch testing. The counterparts were 3 mm diameter Al_2O_3 spheres with an applied load of 10 N over a sliding distance of 5000 m at a relative sliding speed of 0.4 m/s and a track

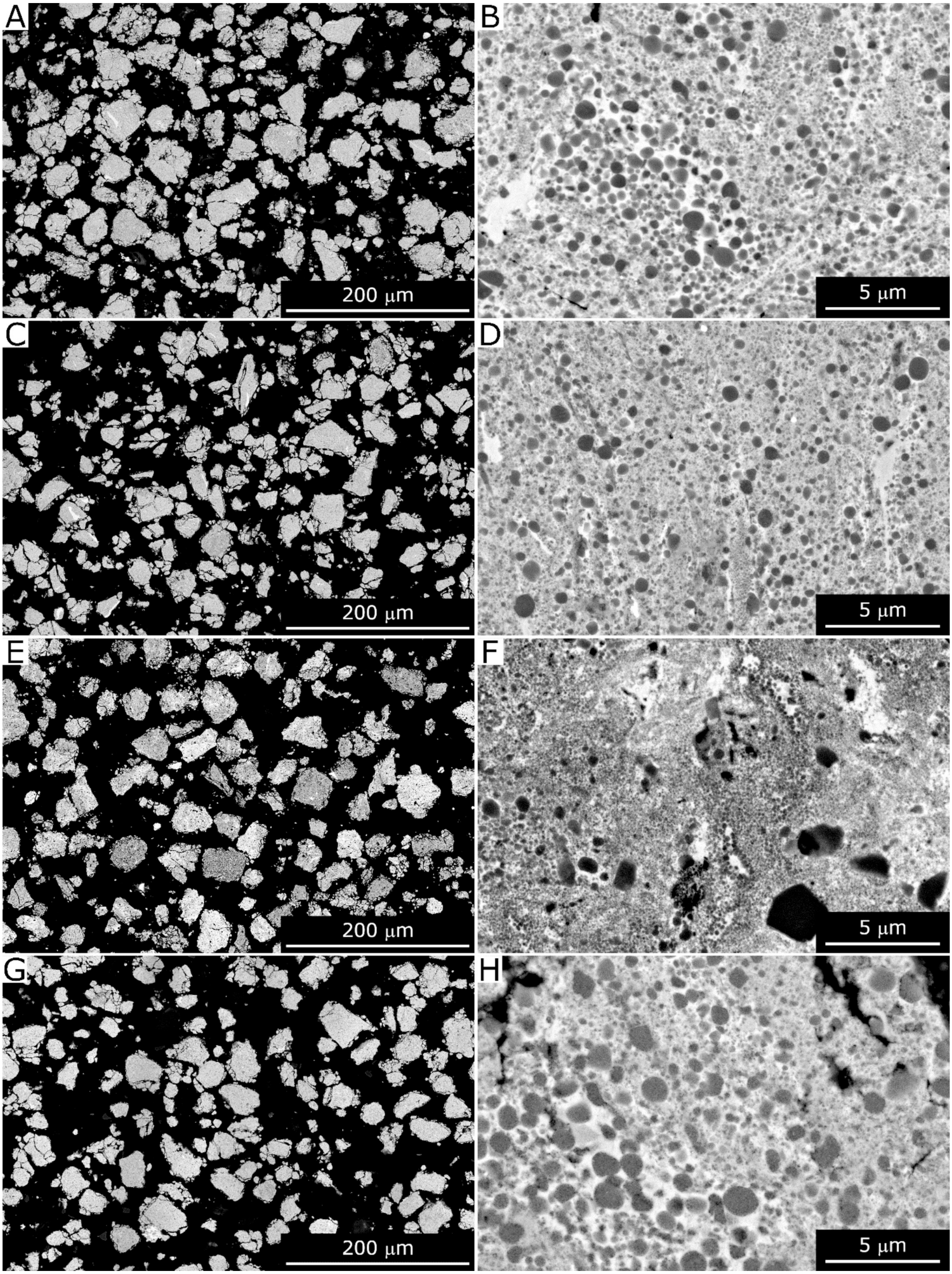

Fig. 1. Backscattered electron SEM micrographs of the HEBM feedstock powders: Cantor+60TiC (A, B), Al_0(CrMnFeNi) + 60TiC (C, D), Al_{14}(CrMnFeNi) + 60TiC (E, F), AlCuCrFeNi+60TiC (G, H). Overviews (A, C, E, G) and details (B, D, F, H).

radius of 7 mm. These conditions were chosen because, based on prior experience with TiC-based hardmetal coatings [57], the combination of a 10 N load and a 3 mm-diameter sphere imposes a sufficiently severe contact condition to reveal any possible issues associated with the brittleness of the material. A hard and chemically inert counterpart such as Al_2O_3 is suitable to simulate a condition of sliding against a hardened surface and/or a surface containing hard asperities, and it avoids additional tribochemical interactions that would complicate the interpretation of the behaviour.

At least two tests were conducted on each sample. The friction coefficient was measured during the test using a load cell. The volumetric wear loss of the ball was assessed by measuring the diameter of the circular wear scar with an optical microscope (Olympus GS30) after the test and calculating the corresponding volume of the worn-out spherical cap. The volumetric wear loss of the coatings was measured using a structured illumination microscopy technique (ConfoSurf profilometer, Confovis GmbH, Jena, Germany, mounted on a Nikon Eclipse LV150N optical microscope), operating with a 10× objective. Wear loss values were then converted to specific wear rates defined as $K = V/(F_N \cdot L)$, where V = volumetric wear loss, F_N = normal force, L = total sliding distance.

As-deposited plates were employed for high-stress abrasion testing using a steel-wheel apparatus (AP87, Ceramic Instruments, Sassuolo, Italy). In fact, high-stress abrasion applications often employ unpolished coatings because low surface roughness is usually not required. The plates were pressed against a 200 mm diameter Fe360A wheel with a load of 40.2 N. The wheel, rotating at 87 rpm, dragged a tangential flow of FEPA80 (≈180 μm average size) Al_2O_3 abrasive from an adjustable orifice set at an outflow rate of 110 g/min. A minimum of three tests were performed on each sample. Volumetric wear loss was measured by acquiring the profile of the wear track using the same ConfoSurf profilometer mounted on the Nikon Eclipse LV150N optical microscope, operating in focus variation mode with a 5× objective and a ring-light illumination source to compensate for the very rough nature of the abraded surface and the small numerical aperture of the objective.

2.3.4. *Characterization of samples after wear testing*

The surfaces and cross-sections of worn samples after ball-on-disc and steel-wheel abrasion tests were observed by SEM + EDX using the same equipment described in Section 2.3.1. Worn surfaces were observed at an inclination angle of 45° to enhance the morphological contrast. Cross-sections prepared by metallographic cutting were hot mounted in a transparent acrylic resin to facilitate the identification of the wear track. In this case, resin-mounted samples were sputter-coated with a ~ 10 nm thick layer of Au to provide the necessary electrical conductivity. The grinding and polishing procedure was the same as in Section 2.3.1.

The identification of compounds formed on the worn surfaces was further carried out by micro-Raman spectroscopy (LabRAM HR Evolution, Horiba Jobin-Yvon). A Nd:YAG laser with a wavelength of 532 nm and a maximum emission power of 100 mW was filtered to 10 % of this maximum power and focused through a 100× objective onto the surface of the sample. Spectra were acquired with a 600 g/mm diffraction grating. Spectra were obtained as the sum of 6 accumulations with a counting time of 20 s each.

3. Results and discussion

3.1. *Size distribution, microstructure, and phase composition of the powders*

Consistent with our previous results [19,44,57] the HEBM powders (Fig. 1) consisted of slightly angular particles, most of which had an equiaxed shape anyway. This morphology is the result of the dynamic equilibrium established during HEBM between the processes of fracturing and welding of the particles to enable the formation of chemically homogeneous aggregates. In any case, the powders possessed sufficient flowability to yield a stable spraying process. The particle size distributions, whose characteristic values are summarized in Table 3, were quite similar to each other and consistent with the nominally expected ones. The Al_0(CrMnFeNi) + 60TiC powder had slightly lower d_{10} and d_{50} values, consistent with the presence of some finer fragments in Fig. 1C, whilst the AlCuCrFeNi+60TiC powder had a marginally narrower particle size distribution compared to the others (smaller $d_{10} - d_{90}$ span).

Table 3
Characteristic values (10th, 50th, and 90th percentiles) of the size distributions of the HEBM feedstock powders.

Powder	d_{10} [μm]	d_{50} [μm]	d_{90} [μm]
Cantor+60TiC	18	35	62
Al_0(CrMnFeNi) + 60TiC	16	31	55
Al_{14}(CrMnFeNi) + 60TiC	18	35	61
AlCuCrFeNi+60TiC	21	33	53

SEM imaging at higher magnification (Fig. 1B, D, F, H) and corresponding EDX maps (provided for the AlCuCrFeNi+60TiC – Fig. 2 – and the Al_0(CrMnFeNi) + 60TiC composition – Fig. 3 – as examples) showed a relatively homogeneous distribution of hard-phase particles, identifiable from their darker contrast in the backscattered-electrons imaging mode. No visible gaps appeared between the hard phase and the surrounding matrix. The size of the hard phase ranged from larger micrometric particles down to sub-micrometric and even nanometric ones. Indeed, the elemental distribution maps of Figs. 2 and 3 displayed a stronger signal of Ti in correspondence with the largest hard-phase particles, but also a distributed Ti signal across the entire mapped area, because the finest TiC particles were too small to be resolved from the surrounding matrix considering the resolution of the map and the finite size of the X-ray generation region.

EDX spectra acquired on selected hard-phase particles (Fig. 4: spectra 1, 2, 5) confirmed that Ti was their main constituent. An occasional impurity of Mo entered the particle analysed in spectrum 1. Some signal from the matrix elements (Cr, Mn, Fe, Ni, and Al) appeared because the X-ray generation region, which under these conditions was estimated by the Esprit software to have an approximate depth of 1.3 μm and a radius of 0.7 μm, extended outside the carbide particles themselves, as also noted above. However, quantitative results (Table 4) suggest that, at least in some cases, like spectrum 2, the proportion of Cr to the other matrix elements (Al, Mn, Fe, Ni) was much higher than it would have been expected from the matrix composition (as seen e.g. in spectrum 4). This means that Cr, which is the element with the second-highest affinity toward C after Ti among those present in the coating (excluding the occasional Mo impurities), might have participated to a small extent in the carbide formation reaction and became dissolved in the TiC structure. Accordingly, in the EDX maps, the signal of elements like Fe (Figs. 2C, 3C) and Ni (Figs. 2G, 3G) dropped systematically where the intensity of Ti was the highest (Figs. 2F, 3F), but the intensity of Cr did not vanish as systematically (Figs. 2D, 3D), meaning that, whilst some TiC particles were almost free of Cr, others contained a bit of this element.

The matrix was relatively homogeneous (Fig. 1B, D, F, H), which means that the impact energy during HEBM was sufficient to trigger the interdiffusion of the metallic elements. However, there were a few residual inhomogeneities, identifiable as streaks of slightly different backscattered electron contrast levels in Fig. 1B, D, F, H. The EDX spectrum 3 showed an example of a Fe-rich area in the $Al_{14}(Cr_{20}Mn_{25}Fe_{40}Ni_{15})$ matrix, but these occurrences were not limited to Fe, nor the $Al_{14}(Cr_{20}Mn_{25}Fe_{40}Ni_{15})$ matrix alone, as they were visible in the magnified views of all powders (Fig. 1B, D, F, H). The maps in Figs. 2 and 3, for example, show that some other matrix areas were enriched in Cr or, in the case of the Al_0(CrMnFeNi) + 60TiC composition, in Mn (Fig. 3H).

The chemical composition of each powder was quite consistent with

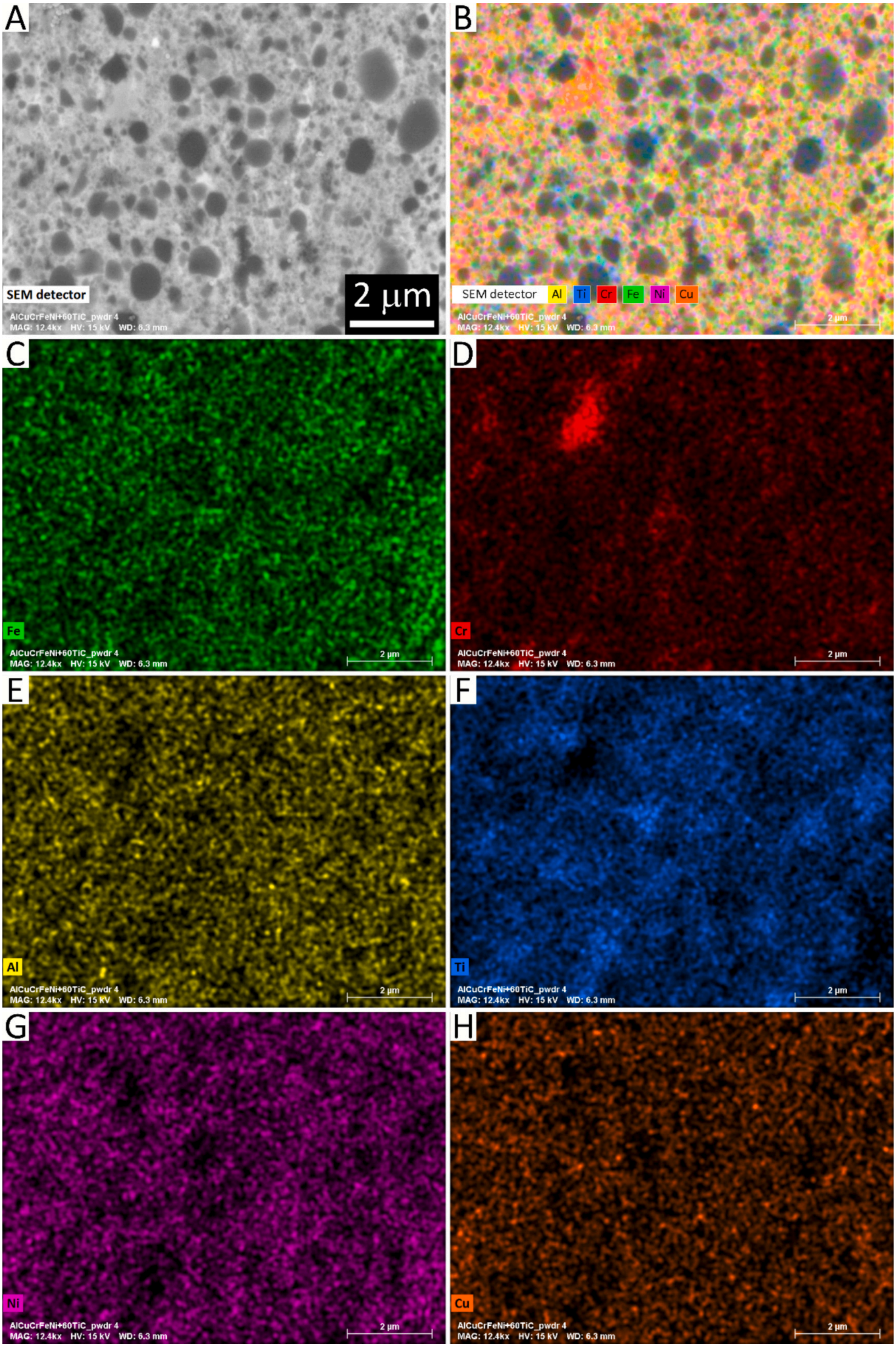

Fig. 2. Backscattered electron SEM micrograph of the AlCuCrFeNi+60TiC powder (A) and elemental distribution maps by EDX: composite map (B) and individual maps of Fe (C), Cr (D), Al (E), Ti (F), Ni (G), and Cu (H).

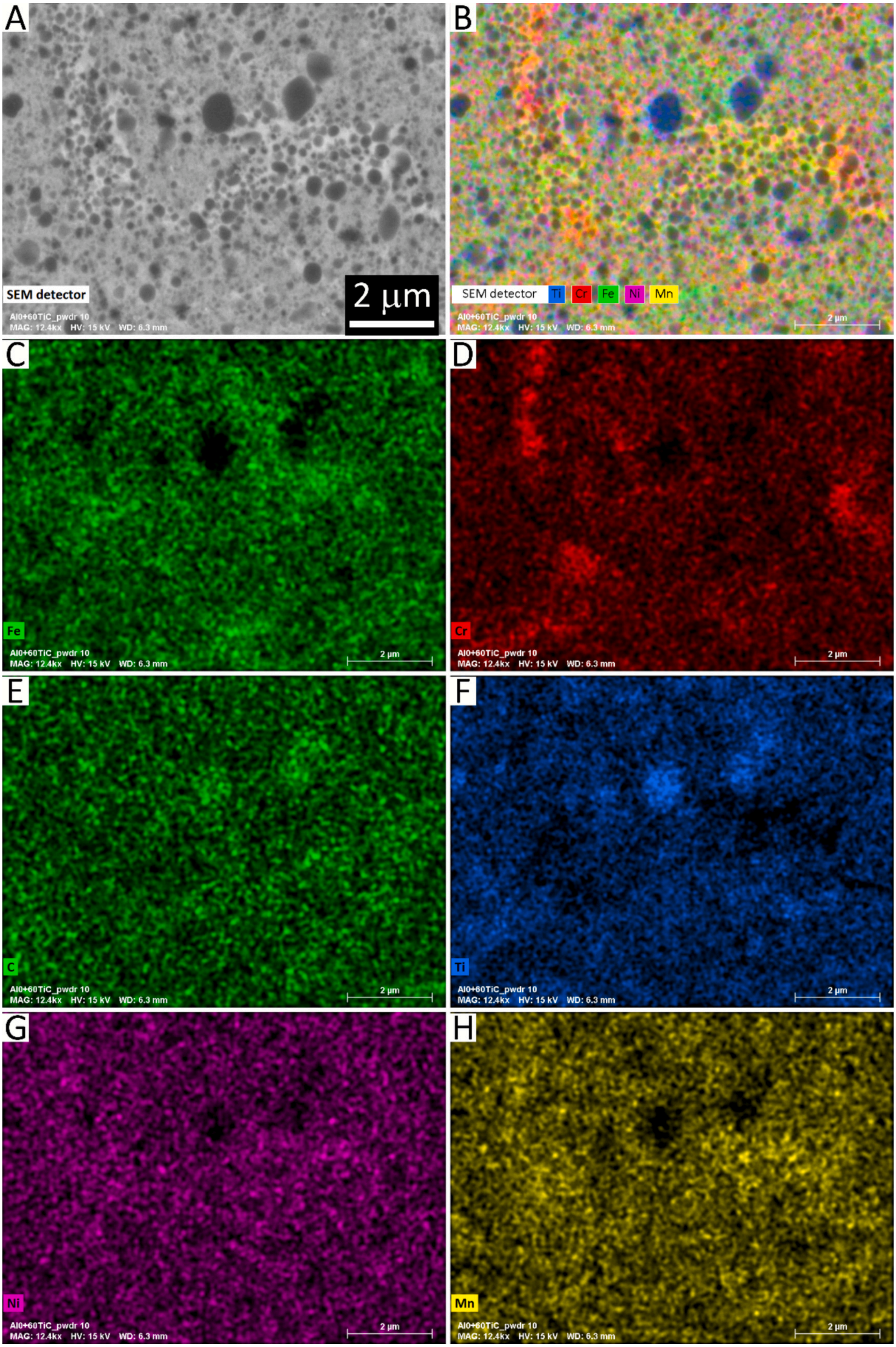

Fig. 3. Backscattered electron SEM micrograph of the Al_0(CrMnFeNi) + 60TiC powder (A) and elemental distribution maps by EDX: composite map (B) and individual maps of Fe (C), Cr (D), C (E), Ti (F), Ni (G), and Mn (H).

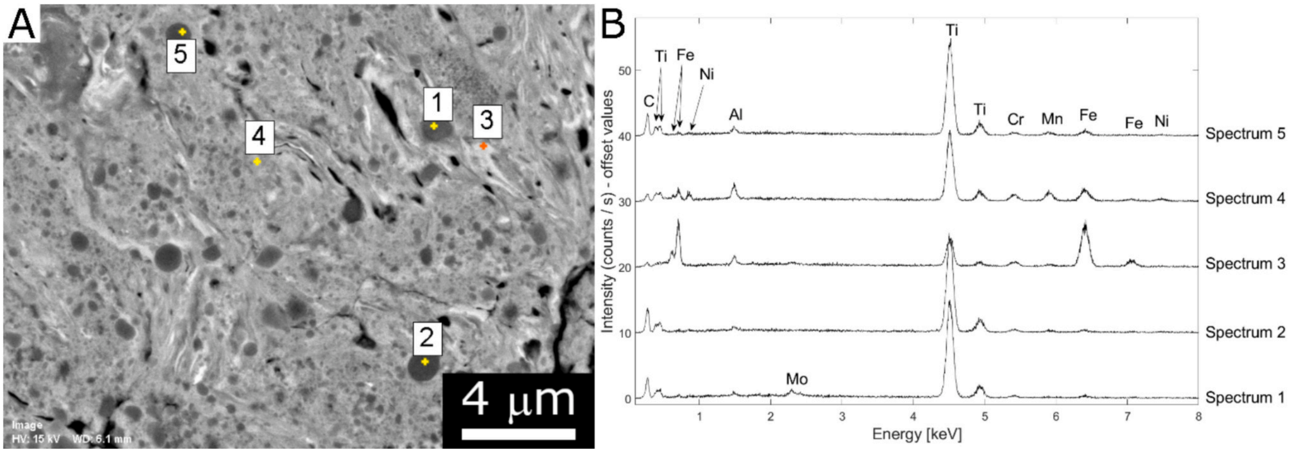

Fig. 4. High-magnification backscattered electron SEM micrograph of the Al_{14}(CrMnFeNi) + 60TiC powder (A) with corresponding EDX spectra (B).

Table 4
Quantitative results from the EDX spectra shown in Fig. 4B, in mass% (normalized to 100).

Spectrum	C	O	Al	Ti	Cr	Mn	Fe	Ni	Mo
1	11.6	1.5	0.7	76.2	2.5	0.4	3.8	0.7	2.5
2	13.8	1.1	0.8	73.2	3.4	2.0	4.2	1.5	0.0
3	2.0	0.4	2.0	17.4	4.1	1.8	70.8	0.7	0.9
4	3.6	1.0	3.3	46.8	7.2	11.6	20.4	6.1	0.0
5	12.3	0.6	1.3	68.5	3.2	3.7	8.2	1.8	0.4

the nominally expected one (Table 5), except for occasional impurities of Mo, W, and Nb, which could have come from residuals of other hardmetal compositions in the production system, and for a generally higher content of Fe in all materials, which could reflect some leftovers from the milling media and/or vials. The carbon and manganese contents in the Al_{14}(CrMnFeNi) + 60TiC powder were also lower than the nominally expected values.

The XRD patterns confirmed that the hard phase, which constituted the primary phase in all powders, had the structure of TiC (Fig. 5). Thus, small amounts of other elements like Cr, which might sometimes have been embedded in the hard phase (as noted above), were dissolved in the cubic TiC lattice and did not trigger the formation of new phases. The signals of unreacted Ti and graphite were not identifiable within the detection limits of the technique (Fig. 5), indicating that the carbide synthesis reaction was completed during the HEBM process, except for the Al_{14}(CrMnFeNi) + 60TiC powder, where in fact a slight carbon deficiency was detected.

Interestingly, it seems that HEBM induced the formation of BCC phase even with matrix compositions, like the CrMnFeCoNi (Fig. 5A) and $Cr_{20}Mn_{25}Fe_{40}Ni_{15}$ (Fig. 5B) alloys, which, as explained in Section 2.1, were thermodynamically expected to contain no or very little such phase, respectively. This can be ascribed to two factors. The high concentration of structural defects induced by the HEBM process, as testified by the large breadth of the diffraction peaks, might have destabilized the densely packed FCC structure and instead favoured a structure with a slightly lower packing density such as the BCC one. Moreover, incomplete homogenization of the matrix elements at the end of the HEBM process left some areas richer in BCC-stabilizing elements such as Fe, as shown previously.

Quantitative assessments by Rietveld refinement (Table 6) returned slightly variable amounts of TiC in the different powders. In particular, it seems that the Cantor+60TiC and the Al_{14}(CrMnFeNi) + 60TiC powders contained a smaller fraction of TiC than was nominally foreseen (see the compositions listed in Section 2.1). It is anyway important to remark that the results from the present Rietveld refinement should be considered as semiquantitative at best and primarily indicative in nature. The accuracy of the Rietveld refinement is indeed influenced by the accuracy with which the structure factor of each phase is known, but this accuracy is limited for the FCC and BCC random solid solutions in HEAs and also for the TiC phase, given the presence of small amounts of substituting elements like Cr, as mentioned above.

Table 5
Overall composition of the powders in mass%, measured by quantitative analysis on EDX spectra acquired on 400× micrographs and elemental analysis. The results were normalized to 100 and are compared to the nominal composition of each material.

Element	Cantor+60TiC		Al_0(CrMnFeNi) + 60TiC		Al_{14}(CrMnFeNi) + 60TiC		AlCuCrFeNi+60TiC	
	Nom.	Measur.	Nom.	Measur.	Nom.	Measur.	Nom.	Measur.
C[a]	9.6	9.27 ± 0.20	9.7	9.34 ± 0.92	10.4	7.10 ± 0.05	9.8	10.44 ± 0.37
N[a]	–	0.19 ± 0.01	–	0.09 ± 0.01	–	0.20 ± 0.01	–	0.10 ± 0.01
O[a]	–	0.75 ± 0.01	–	0.51 ± 0.01	–	0.69 ± 0.02	–	0.39 ± 0.01
Al	–	0.17 ± 0.03	–	0.46 ± 0.07	3.5	3.58 ± 0.23	2.3	2.32 ± 0.17
Ti	38.2	35.75 ± 0.39	38.9	37.61 ± 0.60	41.5	42.34 ± 0.22	39.2	37.40 ± 0.24
Cr	9.7	9.82 ± 0.22	9.7	9.32 ± 0.06	8.4	9.46 ± 0.22	8.8	8.69 ± 0.09
Mn	7.4	8.99 ± 0.11	12.8	11.00 ± 0.34	11.1	6.44 ± 0.05	–	0.67 ± 0.01
Fe	10.4	14.75 ± 0.25	20.8	24.52 ± 0.42	18.0	23.02 ± 0.16	10.7	11.75 ± 0.15
Co	11.0	9.94 ± 0.08	–	–	–	–	–	–
Ni	10.9	10.06 ± 0.04	8.2	7.75 ± 0.37	7.1	6.63 ± 0.27	19.8	17.99 ± 0.45
Cu	–	–	–	–	–	–	9.4	10.25 ± 0.40
Mo	–	–	–	0.32 ± 0.16	–	0.31 ± 0.06	–	–
W	–	–	–	–	–	0.23 ± 0.13	–	–
Nb	–	0.31 ± 0.06	–	–	–	–	–	–

[a] Measured by elemental analysis.

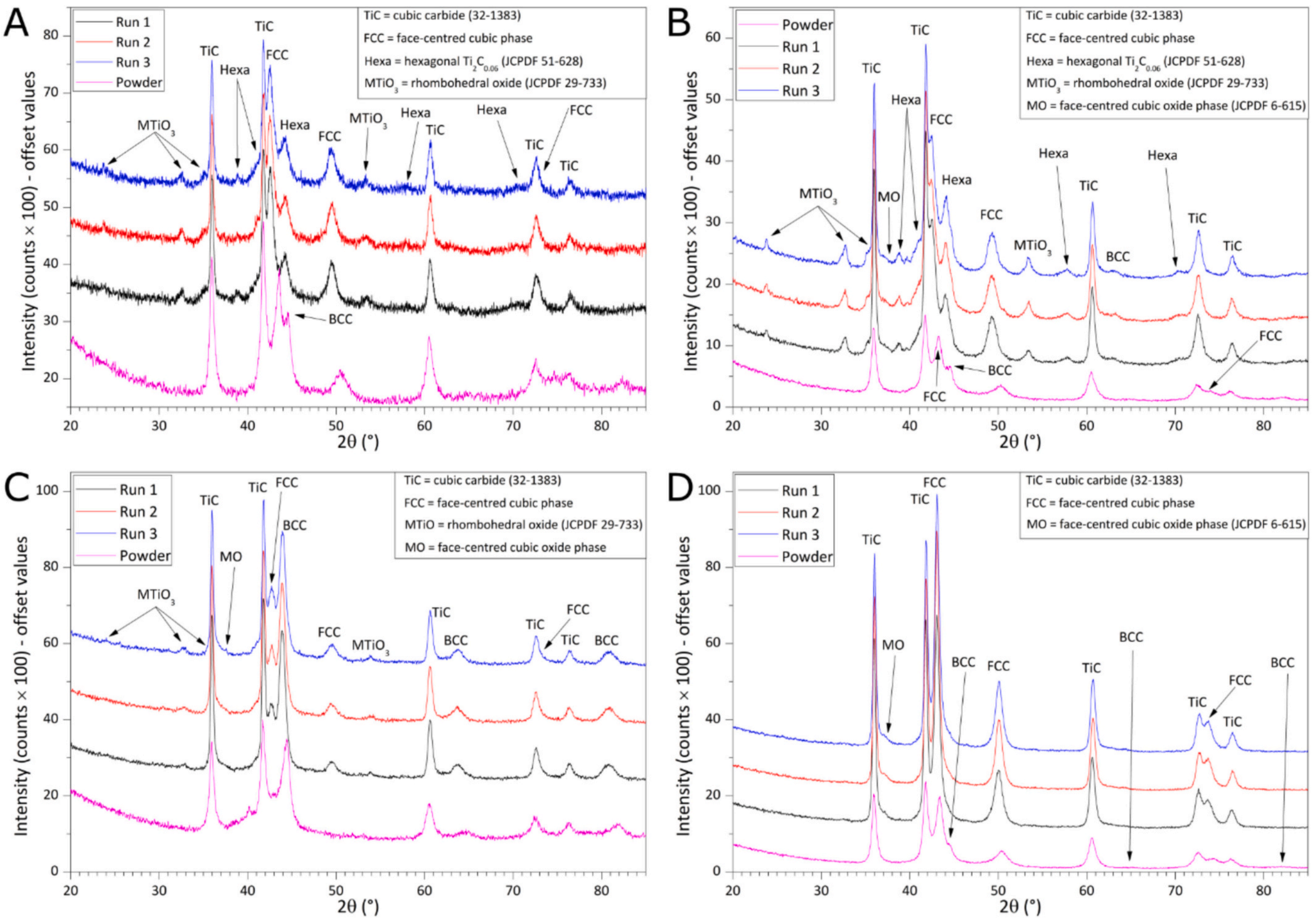

Fig. 5. XRD patterns of the HEBM feedstock powders and the corresponding HVOF-sprayed coatings: Cantor+60TiC (A), Al_0(CrMnFeNi) + 60TiC (B), Al_{14}(CrMnFeNi) + 60TiC (C), AlCuCrFeNi+60TiC (D).

Table 6
Quantitative phase composition (in wt%) of the feedstock powders and the coatings by Rietveld refinement of the XRD patterns.

Sample	FCC	BCC	TiC	Ti	TiC_{1-x}	MO	$MTiO_3$
Cantor + 60TiC powder	52.4 ± 0.3	8.2 ± 0.4	39.4 ± 0.6	–	–	–	–
Cantor + 60TiC Run1	39.6 ± 0.3	–	29.1 ± 0.2	–	23.6 ± 0.4	–	7.7 ± 0.5
Cantor + 60TiC Run2	41.1 ± 0.3	–	28.9 ± 0.2	–	21.8 ± 0.4	–	8.2 ± 0.6
Cantor + 60TiC Run3	37.4 ± 0.3	–	27.8 ± 0.2	–	26.2 ± 0.5	–	8.6 ± 0.6
Al_0(CrMnFeNi) + 60TiC Powder	33.5 ± 0.4	8.8 ± 0.4	57.7 ± 0.2	–	–	–	–
Al_0(CrMnFeNi) + 60TiC Run1	34.5 ± 0.3	2.0 ± 0.1	36.8 ± 0.2	–	15.5 ± 0.4	3.5 ± 0.9	7.7 ± 0.3
Al_0(CrMnFeNi) + 60TiC Run2	31.3 ± 0.2	2.5 ± 0.4	34.4 ± 0.2	–	18.6 ± 0.4	4.0 ± 0.4	9.2 ± 0.3
Al_0(CrMnFeNi) + 60TiC Run3	29.7 ± 0.4	2.5 ± 0.4	33.5 ± 0.2	–	19.8 ± 0.4	4.4 ± 0.9	10.1 ± 0.3
Al_{14}(CrMnFeNi) + 60TiC Powder	7.8 ± 0.3	33.1 ± 0.3	42.9 ± 0.2	16.2 ± 0.7	–	–	–
Al_{14}(CrMnFeNi) + 60TiC Run1	20.5 ± 0.5	27.3 ± 0.3	38.2 ± 0.2	–	3.8 ± 0.5	8.1 ± 0.8	2.1 ± 0.4
Al_{14}(CrMnFeNi) + 60TiC Run2	20.8 ± 0.5	25.7 ± 0.3	36.1 ± 0.2	–	3.9 ± 0.5	10.9 ± 0.9	2.6 ± 0.5
Al_{14}(CrMnFeNi) + 60TiC Run3	20.3 ± 0.4	25.2 ± 0.2	34.1 ± 0.2	–	4.6 ± 0.5	12.4 ± 0.9	3.4 ± 0.5
AlCuCrFeNi + 60TiC Powder	49.7 ± 0.4	1.8 ± 0.2	48.5 ± 0.2	–	–	–	–
AlCuCrFeNi + 60TiC Run1	43.4 ± 0.2	0.5 ± 0.1	46.6 ± 0.1	–	1.1 ± 0.1	7.9 ± 0.5	0.5 ± 0.2
AlCuCrFeNi + 60TiC Run2	44.7 ± 0.2	0.6 ± 0.1	45.4 ± 0.1	–	0.5 ± 0.2	8.5 ± 0.3	0.3 ± 0.1
AlCuCrFeNi + 60TiC Run3	44.3 ± 0.2	0.7 ± 0.6	45.0 ± 0.2	–	0.6 ± 0.1	9.1 ± 0.3	0.4 ± 0.1

3.2. Microstructure and phase composition of the coatings

For each powder composition, the three coatings obtained under the conditions of low, intermediate, and high gas flow rates did not exhibit significant microstructural differences. This can be qualitatively appreciated from Fig. 6 in the case of the Cantor+TiC samples. Quantitative measurements of thickness and porosity (Table 7) confirmed that the differences among the deposition runs were usually small or negligible for the four materials. Therefore, for the sake of brevity, only one representative sample is shown in Fig. 7 for the Al_0(CrMnFeNi) + 60TiC (panels A-C), Al_{14}(CrMnFeNi) + 60TiC (panels D-F), and AlCuCrFeNi+60TiC (panels G-I) coatings. Notably, all coatings exhibited porosity values well below 1 % (Table 7). The porosity of the AlCuCrFeNi+60TiC samples, in particular, was practically not measurable, at least under the "Run1" and "Run2" conditions. This suggests that the samples obtained from this feedstock were particularly dense.

The deposition efficiencies, calculated from the weight change of the samples as described in Section 2.2, were mostly 50 %–60 % (Table 7).

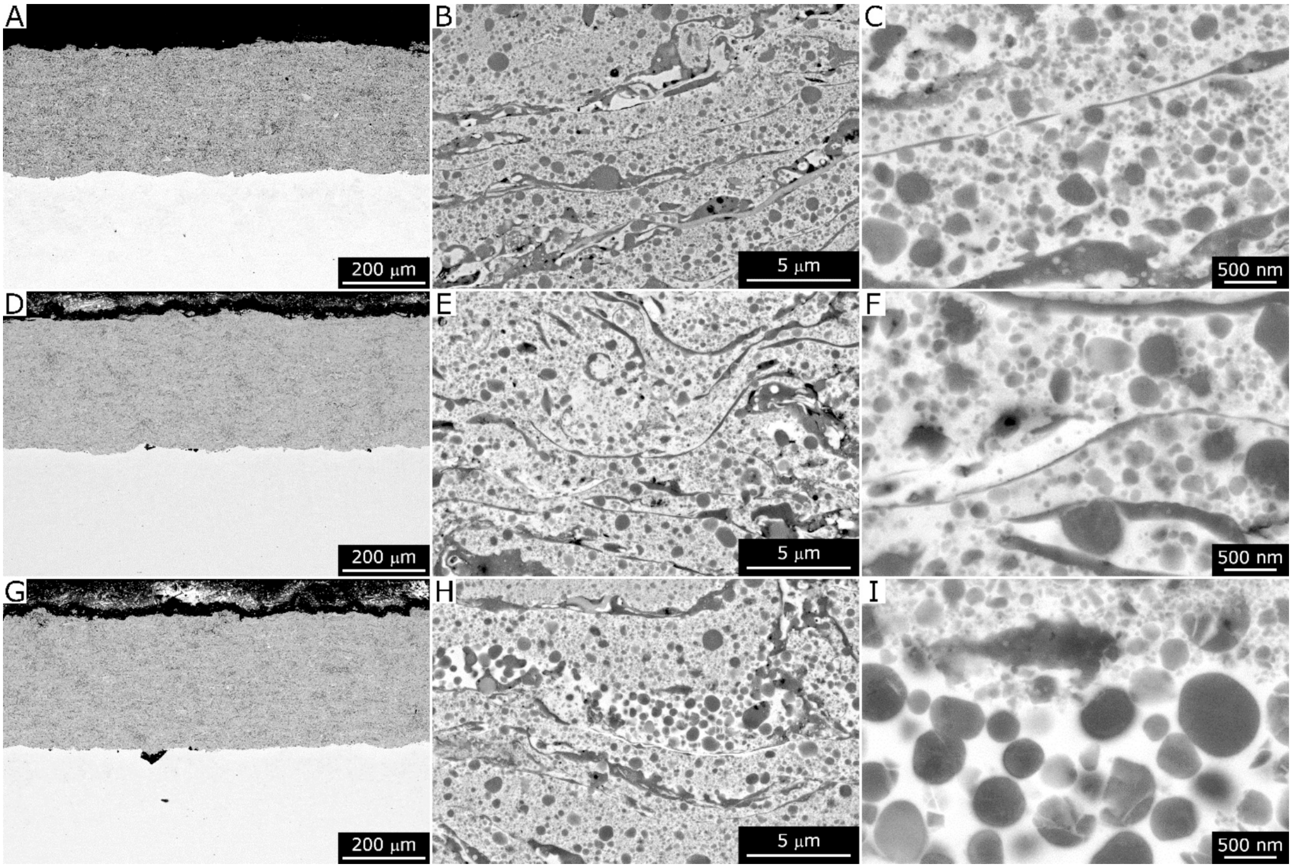

Fig. 6. Backscattered electron SEM micrographs of the Cantor+60TiC coatings: Run1 (A-C), Run2 (D-F), and Run3 (G-I). Overviews (A, D, G), intermediate (B, E, H) and high-magnification (C, F, I) views.

Table 7
Porosity and thickness (mean ± standard deviation) of all coatings by image analysis, and deposition efficiency.

Sample ID	Porosity (%)	Thickness [μm]	Deposition efficiency (%)
Cantor+60TiC Run1	0.38 ± 0.24	294 ± 13	53.0
Cantor+60TiC Run2	0.74 ± 0.49	332 ± 11	60.8
Cantor+60TiC Run3	0.20 ± 0.09	307 ± 11	58.3
Al_{14}(CrFeMnNi) + 60TiC Run1	0.22 ± 0.03	363 ± 10	64.1
Al_{14}(CrFeMnNi) + 60TiC Run2	0.23 ± 0.04	339 ± 8	55.5
Al_{14}(CrFeMnNi) + 60TiC Run3	0.33 ± 0.04	326 ± 11	57.1
Al_0(CrFeMnNi) + 60TiC Run1	0.18 ± 0.03	323 ± 21	59.8
Al_0(CrFeMnNi) + 60TiC Run2	0.21 ± 0.08	310 ± 20	58.7
Al_0(CrFeMnNi) + 60TiC Run3	0.23 ± 0.09	281 ± 18	55.6
AlCuCrFeNi+60TiC Run1	0.17 ± 0.04	321 ± 15	59.9
AlCuCrFeNi+60TiC Run2	0.14 ± 0.04	311 ± 15	56.9
AlCuCrFeNi+60TiC Run3	0.16 ± 0.04	308 ± 13	55.1

Except for the Cantor+60TiC composition, deposition efficiency decreased slightly with increasing gas flow rates (from “Run1” to “Run3” conditions), which could have been a consequence of increased rebounding of particles accelerated to higher impact velocities due to the larger amount of gas flowing through the torch. However, these values can be considered suitable for industrial production, since a similar efficiency of around 60 % was also obtained with the commercial WC-CoCr powder (Section 2.2).

All samples also contained oxide inclusions, recognisable primarily as dark stringers along the lamellar boundaries in the magnified views of Fig. 6B, C, E, F, H, I and Fig. 7B, C, E, F, H, I. EDX analyses (Fig. 8A, B: spectrum 1; Fig. 8C, D: spectra 1, 2; Fig. 8E, F: spectra 1, 2; Fig. 8G, H: spectra 1–3) showed that these oxides were rich in Ti. Their formation may have occurred according to the following mechanism. During the spraying process, the metallic matrix was mainly melted, as indicated by the large degree of flattening of the lamellae seen in the SEM micrographs, and some TiC was probably dissolved in such a matrix. The dissolved Ti then diffused to the outer surface of the particles, either during flight or immediately after deposition [58], to react with oxidizing agents: environmental air entrained in the HVOF jet [59], or water vapour, the main product of the $H_2 – O_2$ combustion. In all the coating systems studied in this work, indeed, Ti was the element with the largest thermodynamic affinity not only toward carbon (which was exploited in the powder manufacturing process as explained above), but also (together with aluminium) toward oxygen.

Qualitatively, it would look like the Al_{14}(CrMnFeNi) + 60TiC composition experienced a slightly higher degree of oxidation (Fig. 7E), whilst the AlCuCrFeNi+60TiC coatings had a comparatively lower oxide content (Fig. 7H), compared to the other two compositions (Figs. 7B and 6B, E, H). Unfortunately, the present samples did not allow quantification of the volumetric fraction of oxide inclusions by image analysis, because the backscattered electrons' contrast level of the oxides was very similar to that of the hard phase. Therefore, they could not be differentiated by greyscale thresholding. However, quantitative analyses by EDX spectroscopy (despite the limitations in quantifying oxygen with this method) suggested that the AlCuCrFeNi+60TiC coatings did have the lowest oxygen contents among all samples, slightly above 5 wt %, whilst the Al_{14}(CrMnFeNi) + 60TiC coatings exhibited the highest ones, above 8 wt% (Table 8). However, oxygen uptake in the HVOF-

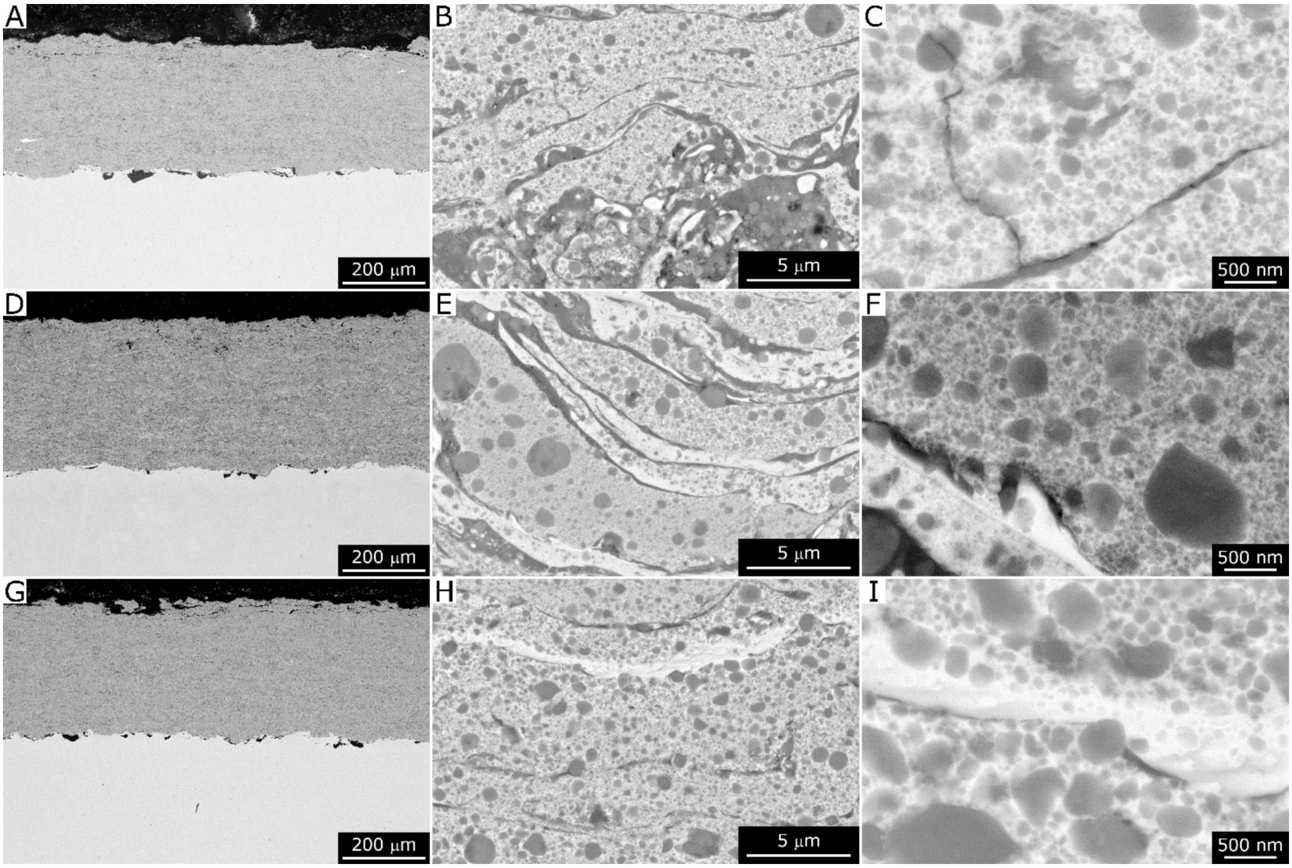

Fig. 7. Backscattered electron SEM micrographs of the Al_0(CrMnFeNi) + 60TiC Run2 (A-C), Al_{14}(CrMnFeNi) + 60TiC Run1 (D-F), and AlCuCrFeNi+60TiC Run1 (G-I) coatings. Overviews (A, D, G), intermediate (B, E, H) and high-magnification (C, F, I) views.

sprayed coatings was quite substantial, compared to the composition of the feedstock powders (Table 4). Besides oxidation, there was no major compositional alteration compared to the composition of the starting powders (compare with Table 5). The ratios among the matrix constituents were indeed mostly the same, and again, a few inclusions of W, Mo, and/or Nb could be detected. However, their amounts were low enough so that no influence on the coatings' properties is expected.

Despite the formation of Ti-based oxides and the related assumptions on the occurrence of some hard-phase dissolution during spraying, the coatings retained most of the TiC particles originally existing in the feedstock, including even the finest ones, as shown in the most magnified views (Figs. 6C, F, I and 7C, F, I). Once again, in some of the carbide particles, the EDX peak of Cr was intensified in comparison to that of the other matrix elements. This is seen for instance in Fig. 8G, H: in spectrum 6, acquired on a carbide particle, the Cr peak is much more intense than those of Fe, Ni and Cu, whilst in spectrum 4, which shows the average composition of a splat, the intensities are much closer to one another. This confirmed the occasional presence of Cr in TiC, as already detected in the powders.

XRD patterns (Fig. 5) also confirmed that the coatings retained face-centred cubic TiC as the primary phase. However, the (semi)quantitative results of the Rietveld refinement (Table 6) indicated that its amount decreased in all cases. Moreover, a peak ascribable to a hexagonal phase of decarburized TiC_{1-x} was also detectable in all coatings (Fig. 5A-C) except for the AlCuCrFeNi+60TiC ones (Fig. 5D). Thus, it is inferred that the decrease in the amount of TiC from the powders to the coatings was due not only to oxidation and dissolution, as commented previously, but also to decarburization. Consistently, the materials that exhibited the largest loss of TiC after spraying were also those with the largest amount of TiC_{1-x}, namely the Cantor+60TiC and Al_0(CrMnFeNi) + 60TiC samples (Table 6). Specifically, in the AlCuCrFeNi+60TiC coatings, even by including the TiC_{1-x} phase in the Rietveld refinement, the resulting amount was around the detection limit of the XRD method itself. This means that the loss of TiC from the powder to the coating was lower than in all other samples.

The role of decarburization is corroborated by the fact that in most cases, the amount of TiC_{1-x} in the coatings was inversely correlated with the carbon loss. That is, the AlCuCrFeNi+60TiC coatings did not exhibit a decrease in carbon content (Table 8) compared to the corresponding feedstock powder (Table 4). In the Al_{14}(CrMnFeNi) + 60TiC coatings, the C content (~6.2–6.4 wt%, Table 8) was slightly lower than in the powder (~7.1 wt%, Table 4). In contrast, the carbon content of the Cantor+60TiC powder (~9.3 wt%, Table 4) decreased to ~7.8–7.9 wt% in the coatings (Table 8), which correspondingly contained around 25 wt% TiC_{1-x} (Table 6). However, this result should be taken with some care in light of the limits in the EDX quantification of a light element such as carbon, with a low electron impact cross-section, in a resin-mounted sample, where some carbon might have been dragged onto the sample during polishing. For instance, the Al_0(CrMnFeNi) + 60TiC samples are partly at odds with the above trends, since they did not exhibit a major carbon loss after deposition (Tables 5, 8) but still contained around 15–20 % TiC_{1-x} (Table 6).

In any case, all the above results pointed to a lower overall degree of carbide alteration in the AlCuCrFeNi+60TiC coatings by any of the possible mechanisms (dissolution, oxidation, and/or decarburisation), since they exhibited minimal loss of TiC, a nearly complete absence of decarburized TiC_{1-x}, and the lowest oxygen content among all coatings. Future research should clarify whether this result came from the slightly narrower particle size distribution of the feedstock powder (Section 3.1), which means that fewer fine particles could have been particularly prone to overheating and oxidation due to their higher surface/volume ratio, or from the different matrix composition. In particular, in terms of

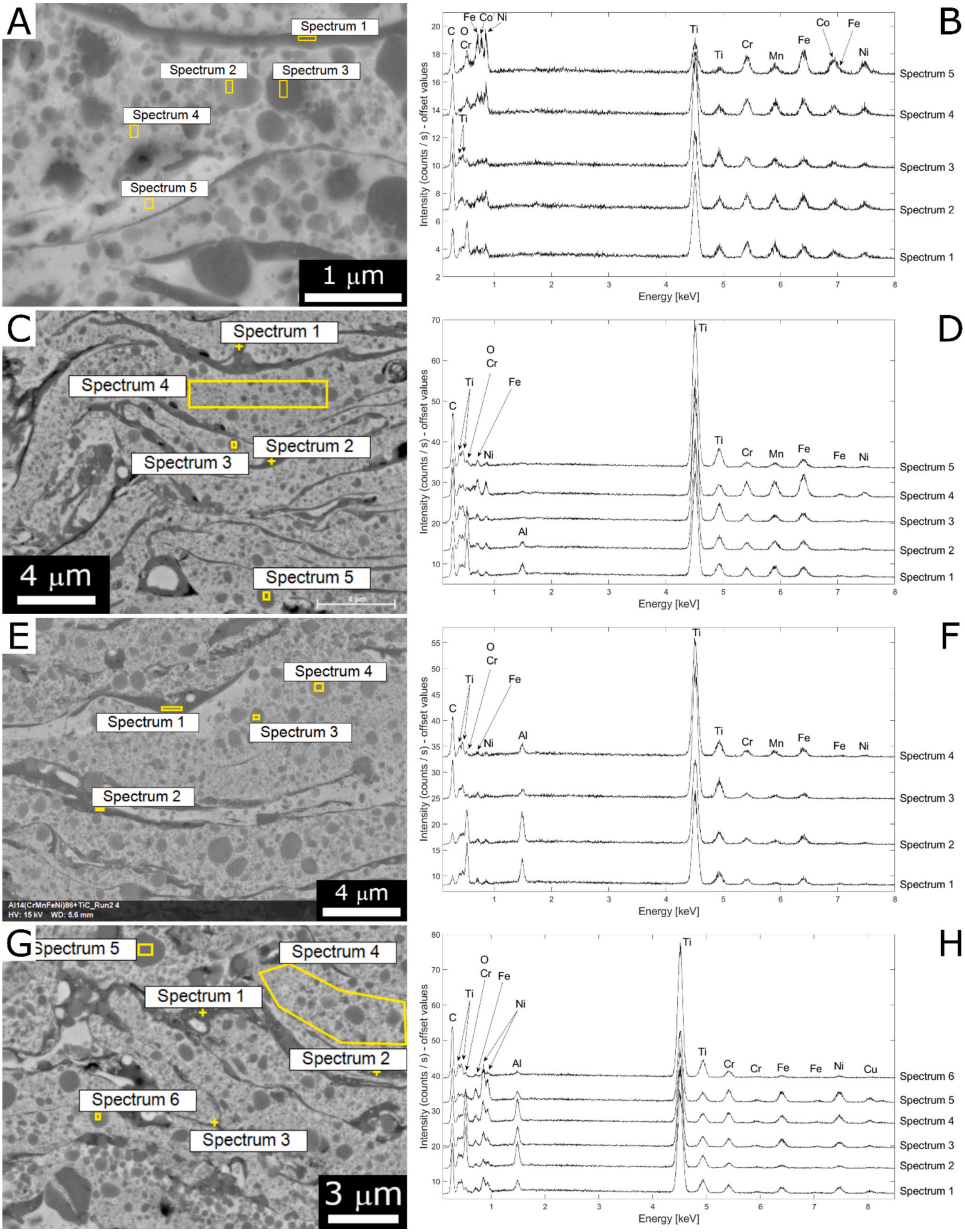

Fig. 8. Backscattered electron SEM micrographs of the Cantor+60TiC Run2 (A), Al_0(CrMnFeNi) + 60TiC Run1 (C), Al_{14}(CrMnFeNi) + 60TiC Run2 (E), and AlCuCrFeNi+60TiC Run3 (G) coatings, with corresponding EDX spectra (B, D, F, H).

Table 8

Chemical composition of the coatings (mass%, normalized to 100) measured by EDX analysis on areas imaged at 400×: mean ± standard deviation.

Element	Cantor+60TiC			Al_0(CrMnFeNi) + 60TiC		
	Run1	Run2	Run3	Run1	Run2	Run3
Carbon	7.94 ± 0.11	7.75 ± 0.02	7.88 ± 0.02	9.89 ± 0.12	9.43 ± 0.07	9.12 ± 0.05
Oxygen	5.45 ± 0.21	5.90 ± 0.26	6.20 ± 0.19	7.70 ± 0.19	7.77 ± 0.06	8.29 ± 0.16
Aluminium	0.07 ± 0.02	0.10 ± 0.04	0.09 ± 0.07	0.40 ± 0.04	0.36 ± 0.03	0.31 ± 0.03
Silicon	0.22 ± 0.03	0.23 ± 0.03	0.20 ± 0.01	0.35 ± 0.01	0.29 ± 0.04	0.26 ± 0.01
Titanium	31.72 ± 0.30	31.78 ± 0.23	31.32 ± 0.03	32.01 ± 0.21	32.37 ± 0.10	32.29 ± 0.26
Chromium	9.64 ± 0.09	9.66 ± 0.13	9.76 ± 0.08	9.05 ± 0.12	9.14 ± 0.08	9.08 ± 0.13
Manganese	8.72 ± 0.08	8.67 ± 0.16	8.45 ± 0.10	8.90 ± 0.13	8.89 ± 0.13	8.59 ± 0.11
Iron	14.91 ± 0.13	14.97 ± 0.05	15.13 ± 0.09	24.06 ± 0.20	24.04 ± 0.20	24.24 ± 0.18
Cobalt	10.37 ± 0.23	10.27 ± 0.07	10.25 ± 0.06	–	–	–
Nickel	10.39 ± 0.04	10.13 ± 0.16	10.21 ± 0.14	7.54 ± 0.17	7.54 ± 0.04	7.62 ± 0.15
Molybdenum	–	–	–	0.10 ± 0.02	0.16 ± 0.02	0.20 ± 0.08
Tungsten	0.12 ± 0.04	0.09 ± 0.04	0.13 ± 0.06	–	–	–
Niobium	0.47 ± 0.04	0.44 ± 0.09	0.40 ± 0.03	–	–	–

Element	Al_{14}(CrMnFeNi) + 60TiC			AlCuCrFeNi+60TiC		
	Run1	Run2	Run3	Run1	Run2	Run3
Carbon	6.44 ± 0.06	6.21 ± 0.06	6.16 ± 0.43	11.44 ± 0.11	10.34 ± 0.11	10.38 ± 0.42
Oxygen	8.20 ± 0.07	8.46 ± 0.28	9.65 ± 0.15	5.39 ± 0.32	5.62 ± 0.17	5.16 ± 0.13
Aluminium	3.04 ± 0.04	3.06 ± 0.04	2.95 ± 0.06	1.93 ± 0.01	1.87 ± 0.03	1.97 ± 0.04
Silicon	0.10 ± 0.03	0.08 ± 0.02	0.12 ± 0.03	0.22 ± 0.01	0.29 ± 0.02	0.08 ± 0.03
Titanium	37.66 ± 0.02	37.64 ± 0.18	37.23 ± 0.35	33.21 ± 0.14	33.28 ± 0.14	33.30 ± 0.23
Chromium	9.02 ± 0.07	9.18 ± 0.07	8.91 ± 0.23	8.41 ± 0.04	8.31 ± 0.04	8.45 ± 0.03
Manganese	5.69 ± 0.09	5.63 ± 0.06	5.04 ± 0.19	0.49 ± 0.06	0.49 ± 0.05	0.48 ± 0.04
Iron	22.61 ± 0.08	22.59 ± 0.32	22.49 ± 0.22	11.40 ± 0.14	11.68 ± 0.26	11.65 ± 0.19
Nickel	6.88 ± 0.09	6.76 ± 0.11	7.06 ± 0.27	17.67 ± 0.15	17.99 ± 0.22	18.35 ± 0.12
Copper	–	–	–	9.83 ± 0.13	10.14 ± 0.15	10.19 ± 0.12
Molybdenum	0.25 ± 0.01	0.32 ± 0.08	0.24 ± 0.02	–	–	–
Tungsten	0.10 ± 0.04	0.07 ± 0.06	0.15 ± 0.02	–	–	–

matrix composition, from the results in Table 6 it seems that the addition of Al was especially conducive to limiting decarburization. The loss of TiC and the formation of TiC_{1-x} were, indeed, lower in the AlCuCrFeNi+60TiC and Al_{14}(CrMnFeNi) + 60TiC compositions than in the others (Table 6).

Looking at the phase composition of the matrix, the HVOF spraying process brought it closer to the nominally expected one, removing the excess BCC phase induced by HEBM. In fact, since most of the metal matrix melted during spraying, there was almost no relation between its phase composition in the powders and the coatings. The phase mix in the coatings even shifted toward a slight excess of the FCC phase.

Namely, there was no detectable BCC phase in the Cantor+60TiC coatings (Fig. 5A), and very little in the Al_0(CrMnFeNi) + 60TiC coatings. Diffraction peaks of the BCC phase were not qualitatively distinguishable in the XRD patterns of the Al_0(CrMnFeNi) + 60TiC coatings Fig. 5B; including this phase in the Rietveld refinement improved the fit quality but the resulting amount was anyway meagre, around 2.0–2.5 wt% (Table 6). This is somewhat consistent with the expectations put forward in Section 2.1. The AlCuCrFeNi+60TiC composition also had an almost pure FCC matrix: once again, the BCC peaks were not discernible in Fig. 5D; inclusion of this phase in the Rietveld refinement yielded concentrations <1 wt%, i.e. around the detection limit. However, a bit of BCC phase could have been expected in this case, as explained in Section 2.1. The matrices of the Al_{14}(CrMnFeNi) + 60TiC coatings contained both BCC and FCC phases (Fig. 5C), with a relative amount of the FCC phase (over the sum of BCC + FCC phases) of approximately 45 % (Table 6). However, no FCC phase was thermodynamically expected. In both cases, the rapid quenching from the melt probably promoted the retention of an FCC structure. Oxidation might also have played a role. The Ti-based oxides of the Al_{14}(CrMnFeNi) + 60TiC coatings tended to include some Al, as seen in Fig. 8E, F: spectra 1, 2 and Fig. 8G, H: spectra 1–3. Even in the Al_0(CrMnFeNi) + 60TiC system, which nominally contained no Al, an Al peak did emerge in the oxides (Fig. 8C, D - spectra 1, 2): this stemmed from the presence of a slight amount of Al as an impurity in the material, as testified by Table 8. Thus, among the matrix elements, Al tended to oxidize preferentially, and this might have resulted in a slight loss of this element from the metal alloy. Therefore, the composition of the Al_{14}(CrMnFeNi) alloy could have been slightly skewed toward the formation of the FCC phase, as the loss of Al implies an increase in both the VEC and the φ parameter (Section 2.1). However, the presence of very finely distributed nanosized TiC prevented a detailed compositional analysis of the matrix phase alone in powders and coatings.

Oxides were also identifiable in the XRD patterns of the Cantor+60TiC, Al_0(CrMnFeNi) + 60TiC and Al_{14}(CrMnFeNi) + 60TiC coatings (Fig. 5A, B, C, respectively). They appeared mainly in the form of a substoichiometric Ti_2O_3 oxide and/or an ilmenite-type $MTiO_3$ structure, with M = transition metal elements such as Fe or Ni, and of a cubic MO phase structurally similar to wüstite. There were no Al oxides within the detection limits of XRD, which implies that Al entered the ilmenite structure.

Unfortunately, since Ti_2O_3 and ilmenite-type $MTiO_3$ are isomorphic, it was not possible to differentiate between them by XRD. The Raman spectra acquired on the oxide inclusions (Fig. 9) also did not provide definitive indications. The Raman signal was indeed consistent with both Ti_2O_3, identified by comparison with the reference spectrum of this phase listed in the RRUFF open database [60], and/or $MTiO_3$ [61], with a possible minor contribution from spinel-type oxides (not seen in the XRD patterns). For the Rietveld refinement, an ilmenite-type $MTiO_3$ phase was assumed. Although this assumption certainly contributed to the approximate nature of the quantitative results, as already discussed in Section 3.1, it is nonetheless possible to note a definite difference between the Al-containing and Al-free compositions (Table 6). Al-free compositions contained a more considerable amount of $MTiO_3$ and comparatively less MO, or even no detectable MO, as in the case of Cantor+60TiC samples. The opposite was true for the Al-containing coatings. The influence of Al on the oxidation process might also have offered some protection against the oxidation of carbon, which was probably the primary mechanism by which decarburization of TiC to hexagonal TiC_{1-x} occurred. This would be consistent with the reduced decarburization degree of the Al-containing formulations, although, as mentioned previously, this aspect should be investigated in more detail.

3.3. Micro- and nano-mechanical properties

Vickers microindentation tests showed that the hardness values of the HEA-based coatings were roughly in the range of 750 to 900 HV (Table 9). This is comparable to or slightly lower than the values usually reported for HVOF Cr_3C_2-NiCr coatings [57,62–67] but lower than the

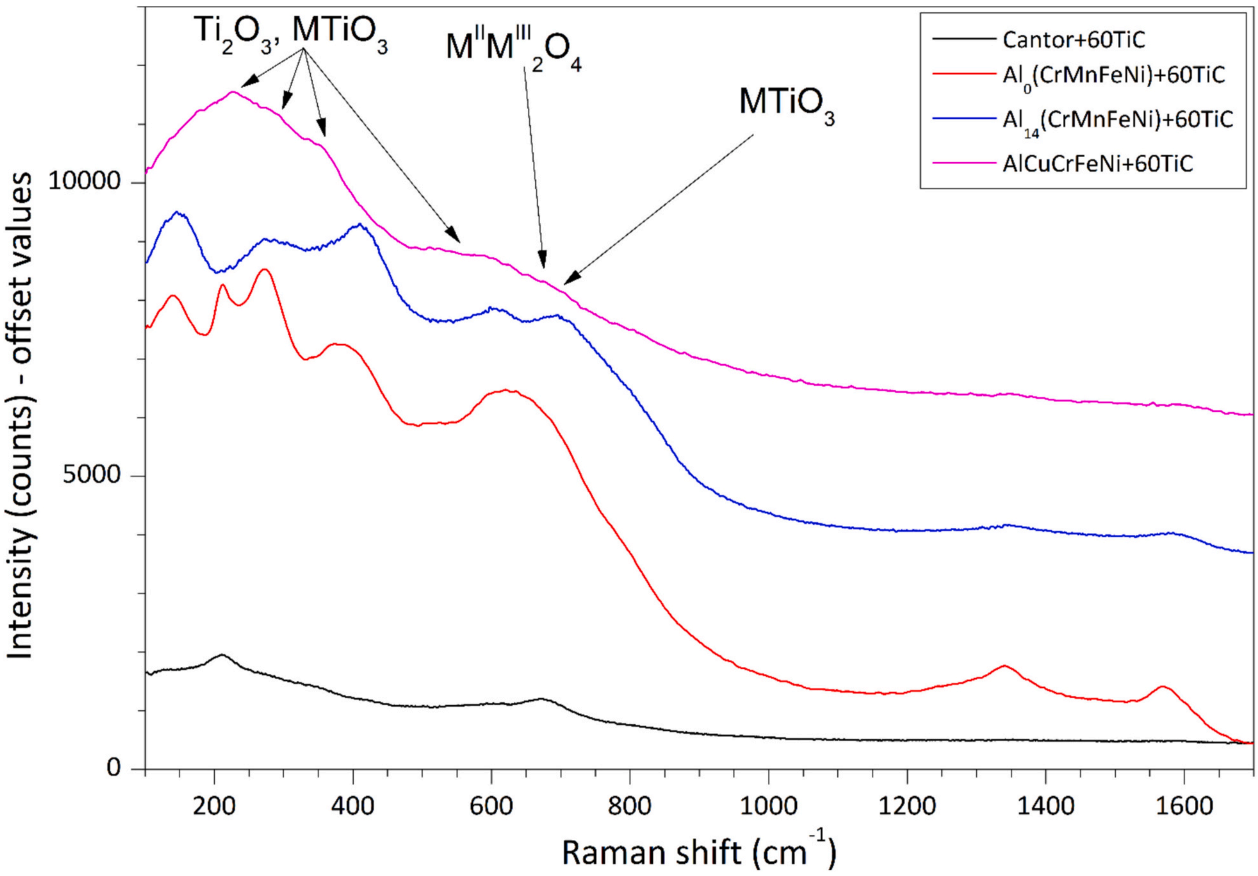

Fig. 9. Micro-Raman spectra acquired on the oxide inclusions in samples Cantor+60TiC Run1, Al_0(CrMnFeNi) + 60TiC Run1, Al_{14}(CrMnFeNi) + 60TiC Run1, and AlCuCrFeNi+60TiC Run1.

Table 9
Vickers microhardness (HV) and elastic modulus (E_{IT}) by depth-sensing Vickers microindentation, and critical loads (L_C) by scratch testing (mean ± standard deviation).

Sample	HV_{3N}	E_{IT} [GPa]	L_C [N]
Cantor+60TiC Run1	884 ± 91	283 ± 20	12.1 ± 1.3
Cantor+60TiC Run2	933 ± 102	302 ± 67	13.4 ± 1.5
Cantor+60TiC Run3	904 ± 97	286 ± 14	13.4 ± 1.4
Al_0(CrMnFeNi) + 60TiC Run1	745 ± 81	338 ± 33	8.7 ± 0.7
Al_0(CrMnFeNi) + 60TiC Run2	786 ± 82	372 ± 31	9.0 ± 1.0
Al_0(CrMnFeNi) + 60TiC Run3	816 ± 70	270 ± 22	10.1 ± 0.6
Al_{14}(CrMnFeNi) + 60TiC Run1	747 ± 80	177 ± 12	12.0 ± 1.4
Al_{14}(CrMnFeNi) + 60TiC Run2	813 ± 60	186 ± 11	9.4 ± 2.0
Al_{14}(CrMnFeNi) + 60TiC Run3	740 ± 73	169 ± 12	10.0 ± 1.6
AlCuCrFeNi+60TiC Run1	772 ± 78	246 ± 18	13.6 ± 2.3
AlCuCrFeNi+60TiC Run2	793 ± 64	249 ± 15	14.6 ± 2.1
AlCuCrFeNi+60TiC Run3	819 ± 77	294 ± 17	13.0 ± 1.1
WC-CoCr	1484 ± 109	455 ± 16	19.8 ± 2.4

hardness (close to 1500 HV) of the WC-CoCr reference. The Cantor+60TiC coatings were, on average, harder than the others, as they were the only samples that showed hardness in the range of 900 HV, while the others were all in the range of 750–800 HV. Elastic moduli were around 250–300 GPa (Table 9), except for the Al_{14}(CrMnFeNi) + 60TiC coatings, which exhibited elastic moduli <200 GPa. This difference did not seem to correlate with porosity, since the porosity of the Al_{14}(CrMnFeNi) + 60TiC coatings was not higher than that of the Cantor+60TiC coatings (Table 7), which, however, exhibited a higher modulus. The difference in elastic modulus did not seem to correlate well with the amount of TiC in the coatings, either: the Al_{14}(CrMnFeNi) + 60TiC samples contained even more TiC than the Cantor+60TiC ones (Table 6). Therefore, the most likely remaining explanation is that the Al_{14}(CrMnFeNi) + 60TiC coatings were somewhat more brittle than the others. The elastic modulus is not, by itself, a measure of toughness, but in the case of thermal spray coatings, previous research by the authors showed that the depth-sensing indentation technique tends to return lower moduli for brittle samples which, by failing inelastically during the indentation process, produce a lower apparent modulus value in the measurement [68].

Differences in toughness among the samples could be more confidently assessed by scratch tests. Based on our previous work on TiC-based hardmetals, indeed, differences in critical loads found by scratch testing in progressive loading mode correlate quite well with the tendency to exhibit brittle fracture under functional testing conditions like the abrasion test [57].

Inspection of the scratch tracks by optical microscopy (Fig. 10) showed that the critical load (L_C) of these samples corresponded to the onset of systematic chipping of the coating along the sides of the track. It is essential to differentiate between isolated events, as also defined in ISO 20502, i.e. localized failures not followed by a systematic continuation of damage, and the actual critical load, i.e. the onset of continuous damage whose severity increases with load, as exemplified by the magnified views from Fig. 10A in the case of the Cantor+60TiC Run2 sample. Isolated failures were due to the unavoidable inhomogeneity of a thermal spray coating, which contains randomly distributed weak spots, such as pores or poorly bonded splats, where localized premature failure could occur. When accounting for this possibility, it is immediately apparent from Fig. 10 that the Cantor+60TiC coatings (panel A) and AlCuCrFeNi+60TiC coatings (panel D) exhibited significantly higher critical load for the onset of chipping than the Al_0(CrMnFeNi) + 60TiC (panel B) and Al_{14}(CrMnFeNi) + 60TiC (panel C) samples.

This was quantitatively confirmed by the mean L_C values in Table 9:

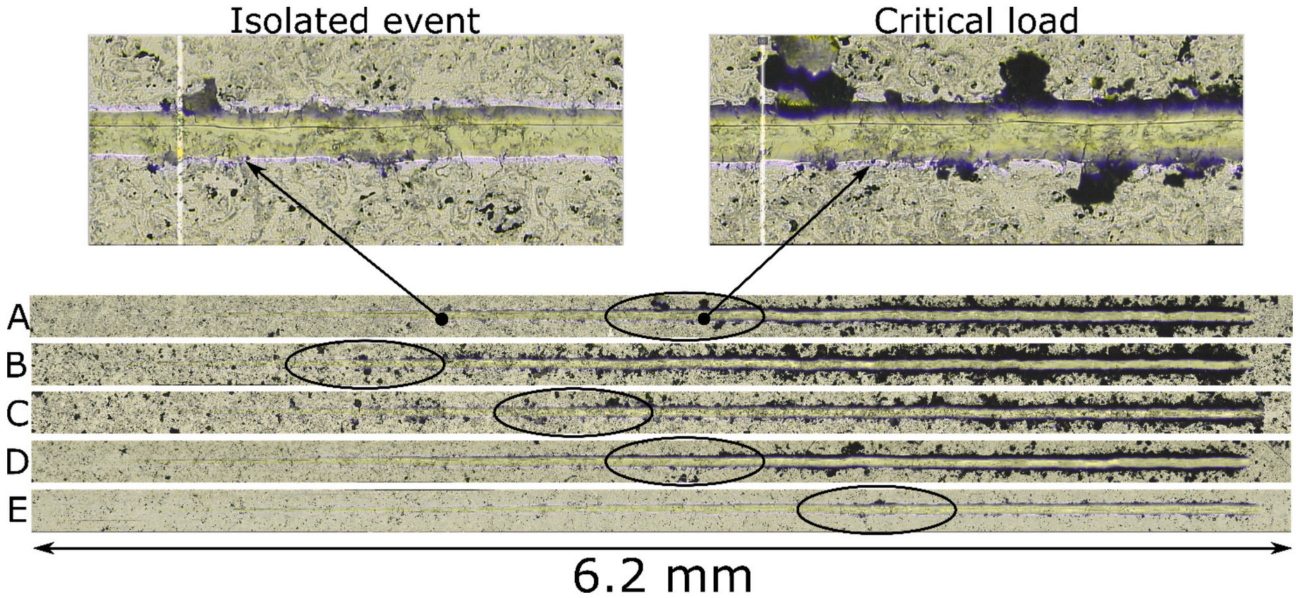

Fig. 10. Stitching of optical images showing overviews of scratch tracks on Cantor+60TiC Run2 (A), Al_0(CrMnFeNi) + 60TiC Run2 (B), Al_{14}(CrMnFeNi) + 60TiC Run1 (C), AlCuCrFeNi+60TiC Run2 (D), and the WC-CoCr reference (E). The circles indicate the region of the critical load. The magnified details show the difference between an isolated event caused by local inhomogeneities and the "true" critical load.

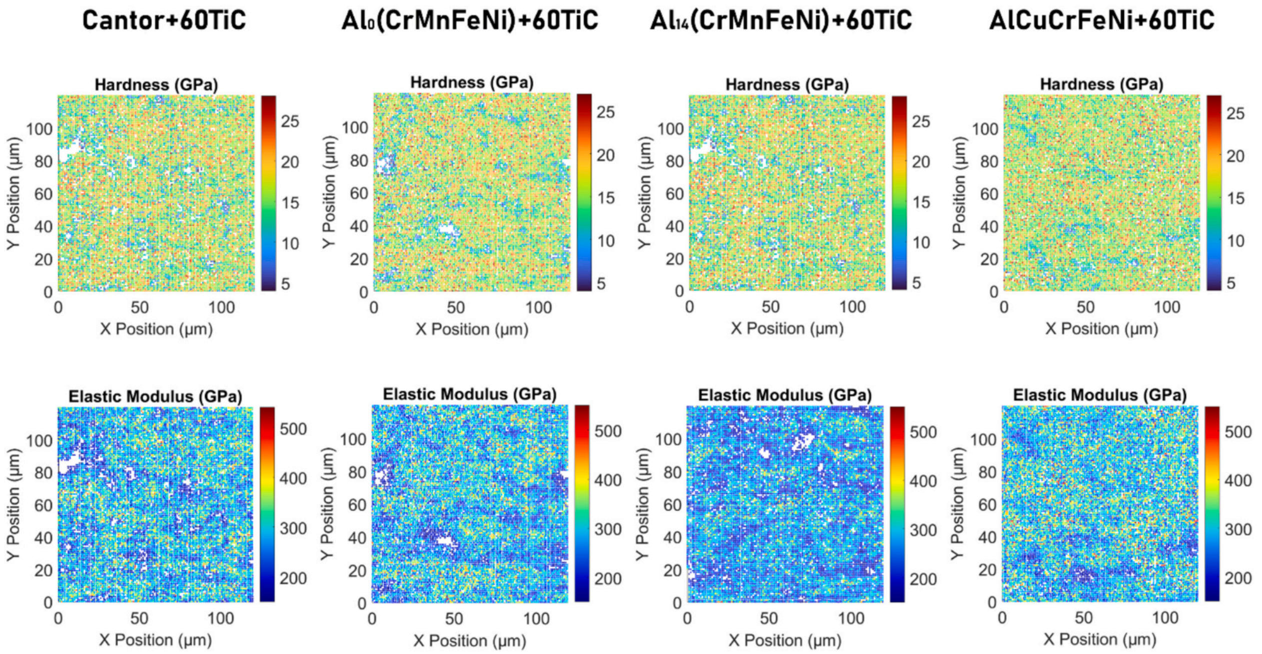

Fig. 11. Hardness and elastic modulus maps obtained by high-speed nanoindentation with 1 μm spacing between indents. Note: the represented areas are cropped from the actual map sizes, and all samples were standardized to the same region of interest (ROI) to illustrate comparative differences effectively.

in most cases, the Al_0(CrMnFeNi) + 60TiC and Al_{14}(CrMnFeNi) + 60TiC samples exhibited critical loads in the range of 8–10 N, whilst the Cantor+60TiC and AlCuCrFeNi+60TiC coatings exhibited L_C values of 12–14 N. Thus, it is indeed confirmed that the Al_{14}(CrMnFeNi) + 60TiC samples tended to be quite brittle and it was also revealed that the same was true for the Al_0(CrMnFeNi) + 60TiC samples. In any case, it was seen that the reference WC-CoCr sample had a higher critical load than all other coatings (Table 9, Fig. 10), and likewise a HVOF-sprayed Cr_3C_2-25 wt%(Ni-20wt.%Cr) coating tested under identical conditions in [57] also exhibited a higher critical load of 16.0 ± 0.1 N. On the other hand, the critical load of HVOF-sprayed (Ti,Mo)(C,N)-25wt.%Ni, tested in the same work [57], was 12.9 ± 0.2 Ni, i.e. it was comparable to the results obtained with the HEA samples. In particular, the AlCuCrFeNi+60TiC samples appeared to have a slightly higher critical load than (Ti,Mo)(C,N)-25wt.%Ni.

A better understanding of the fine-scale mechanical properties of the HEA-based coatings was also obtained by high-speed nanoindentation on selected samples (Fig. 11). The large number of indents performed with this technique, indeed, allowed individual mechanical phases to be identified by the GMM algorithm in the overall distributive plot of the data, as reported in Fig. 12. In this case, mechanical phases can be considered as regions in the material that are homogeneous and not necessarily related to the actual microstructural phases. The results provided in Table 10 show that four mechanical phases could be

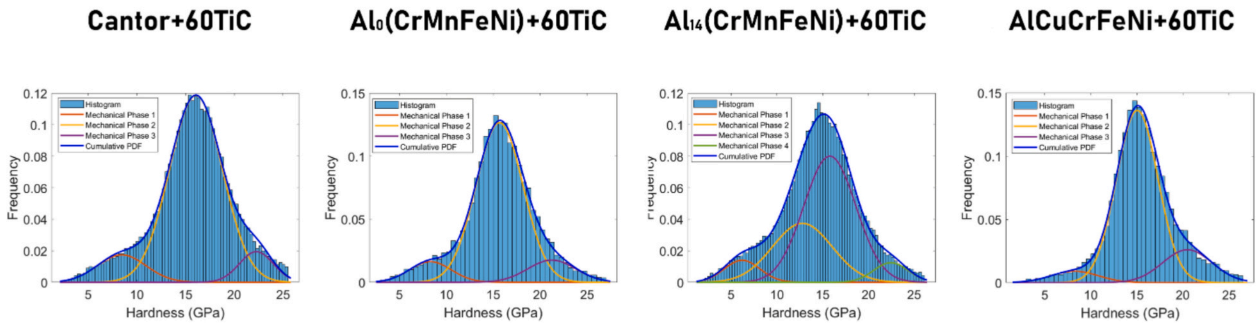

Fig. 12. Distributive curves of indentation hardness obtained by high-speed nanoindentation on the four samples, analysed with the GMM algorithm: in each image, the histogram with the fraction of indentations included in each range of values, the overall histogram-fitting curve (“Cumulative PDF”), and the Gaussian fit of individual distributions (each labelled as a “Mechanical Phase”) are shown.

Table 10
Results of GMM deconvolution to identify mechanical phases from high-speed nanoindentation data.

	Mechanical phase 1		Mechanical phase 2		Mechanical phase 3		Mechanical phase 4	
	E (GPa)	H (GPa)	E (GPa)	H (GPa)	E (GPa)	H (GPa)	E (GPa)	H (GPa)
Cantor +60TiC Run3	168.70 ± 34.23	8.43 ± 2.49			269.96 ± 50.24	16.06 ± 2.71	370.02 ± 35.50	22.26 ± 1.75
Al_0(CrMnFeNi) +60TiC Run3	206.59 ± 37.16	8.29 ± 2.23			276.44 ± 50.75	15.66 ± 2.51	391.20 ± 28.98	21.23 ± 2.56
Al_{14}(CrMnFeNi) +60TiC Run3	142.84 ± 20.30	6.20 ± 1.96	216.11 ± 32.66	12.77 ± 3.24	275.16 ± 33.48	15.78 ± 2.84	346.41 ± 18.78	22.44 ± 1.88
AlCuCrFeNi +60TiC Run3	221.14 ± 40.87	8.27 ± 1.70			283.52 ± 53.59	15.03 ± 2.17	398.78 ± 26.8	20.51 ± 2.20

identified from the data for Al_{14}(CrMnFeNi) + 60TiC. This sample is chosen as an exemplary reference due to its general and comprehensive mechanical behaviour, allowing a discussion of the mechanical phases and their coupling to microstructural features to be applied to other samples, except for the BCC phase, which uniquely arose from the high Al content in the Al_{14}(CrMnFeNi) composition. The first mechanical phase, with an average nanohardness value of ~6.2 GPa, could be assumed to correspond to indents on the softer and more ductile FCC microstructural phase of the matrix. The second mechanical phase, with a value of H ~12.8 GPa, reflected the properties of the harder BCC phase. The third mechanical phase, which was also the one containing most of the data (see Fig. 12), likely corresponded to indents that affected both the matrix and the nano- or submicron-sized TiC particles, yielding an intermediate hardness value of ~15.8 GPa. This is a typical result for high-speed nanoindentation [52], where a vast number of experiments, combined with advanced data analysis, allows including and eventually distinguishing (in a statistically robust way) within the mechanical response the spurious (interfacial) measurements and the actual phases. Ultimately, for that sample, the fourth mechanical phase corresponded to indents falling entirely on the largest, micrometre-sized carbide particles and therefore reflected their mechanical properties, with a hardness of ~22.4 GPa. This value was close to the lower limit of the range of ~2600–3200 HV given for TiC in the literature [69,70]. The consistency with the literature demonstrates the reliability of this analysis, also considering that the present measurement was probably not entirely free of influences by the surrounding matrix.

As seen in Table 10, with a purely (or almost purely) FCC matrix, the second distribution could not be found, whilst the average hardness associated with the first distribution (FCC phase) and the fourth one (TiC particles) was always approximately the same, corroborating to the assignment of these distributions. These results showed, among other things, that the properties of the synthesized TiC phase were substantially independent of the surrounding matrix.

Notably, the nanohardness values of the FCC and BCC phases, as listed above, were much higher than the typical hardness values of bulk HEAs, which are in the range of 150–200 HV and 500–650 HV for purely FCC and BCC materials, according to the extensive database compiled by Gorsse et al. [71]. This can be ascribed to three factors:

1. The indentation size effect, because of which the hardness values measured in metals at low penetration depths in a nanoindentation test were higher than the asymptotic high-load value [72].
2. Probably, even the nanoindentations that fell mainly on a purely metallic (BCC or FCC) area were affected to some degree by the presence of finely distributed TiC particles and/or of the decarburized TiC_{1-x} phase. These two phases were likely to be always present, in smaller or greater amounts, within the plastically deformed volume around and below the indenter, even at low penetration depths.
3. Finally, it is worth mentioning that high-speed nanoindentation achieved higher strain rates than typical quasi-static testing (typically around 3 $1/s$) [52]. This affected the strain rate-sensitive phases, typically resulting in higher elastic modulus and hardness values. For instance, CoCrFeMnNi-based HEAs, such as the present “Cantor” composition, are recognized for their strain rate sensitivity, with the strain response also influenced by factors such as temperature and grain size [73].

The higher hardness of the BCC phase in the Al_{14}(CrMnFeNi) + 60TiC composition, which is probably associated with a lower ductility, may explain the lower toughness of these coatings in the scratch test. Another factor that can explain the behaviour of both the Al_{14}(CrMnFeNi) + 60TiC and the Al_0(CrMnFeNi) + 60TiC compositions is their higher Fe content. Previous work with simple alloys has accordingly shown that hardmetals with Fe-rich matrices are more brittle than those with Ni-rich matrices [19,44,45]. Therefore, this behaviour recurs instead systematically and is expected in both HEA and non-HEA formulations.

3.4. Sliding and abrasive wear behaviour

In terms of both sliding (Fig. 13) and abrasive (Fig. 14) wear

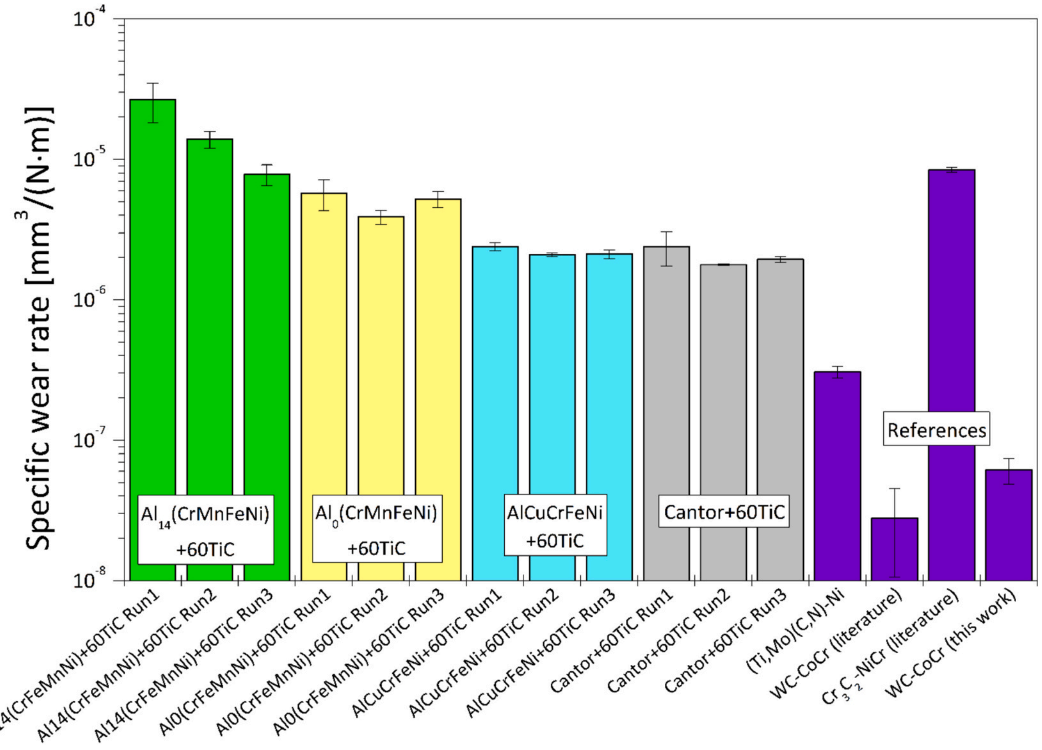

Fig. 13. Specific wear rates measured by ball-on-disc testing on all hardmetal coatings, compared to reference data measured under similar conditions in [57] for (Ti,Mo)(C,N)-Ni and [45] for WC-CoCr and Cr_3C_2-NiCr.

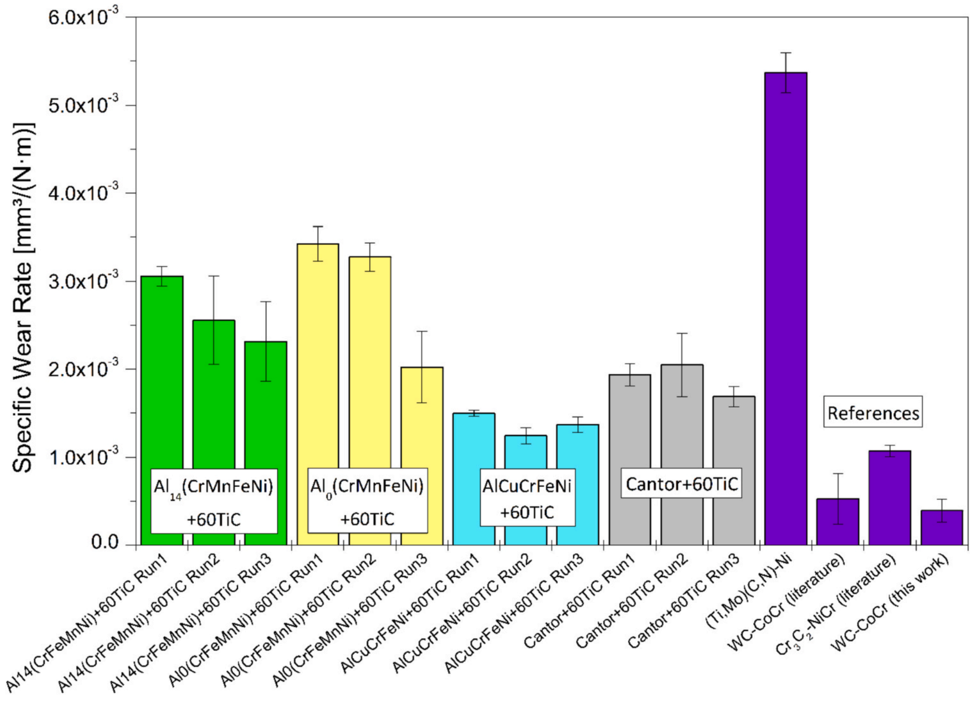

Fig. 14. Specific wear rates measured by steel-wheel abrasion testing on all hardmetal coatings, compared to reference data measured under identical conditions in [57] for (Ti,Mo)(C,N)-Ni and [45] for WC-CoCr and Cr_3C_2-NiCr.

resistance, the coatings notably ranked quite in accordance with their scratch responses. The Al_0(CrMnFeNi) + 60TiC and Al_{14}(CrMnFeNi) + 60TiC compositions, regardless of the deposition parameters, produced higher specific wear rates than the Cantor+60TiC and AlCuCrFeNi+60TiC compositions.

Under sliding wear conditions, the Al_0(CrMnFeNi) + 60TiC (Fig. 15C, D) and Al_{14}(CrMnFeNi) + 60TiC (Fig. 15E, F) coatings exhibited extensive micropitting (some micropits are circled in the micrographs). Thus, surface fatigue was their main wear mechanism. Fatigue is certainly faster in a more brittle material, where energy dissipation by plasticization at the tip of an advancing crack is limited and therefore crack growth is easier. On the contrary, the comparatively

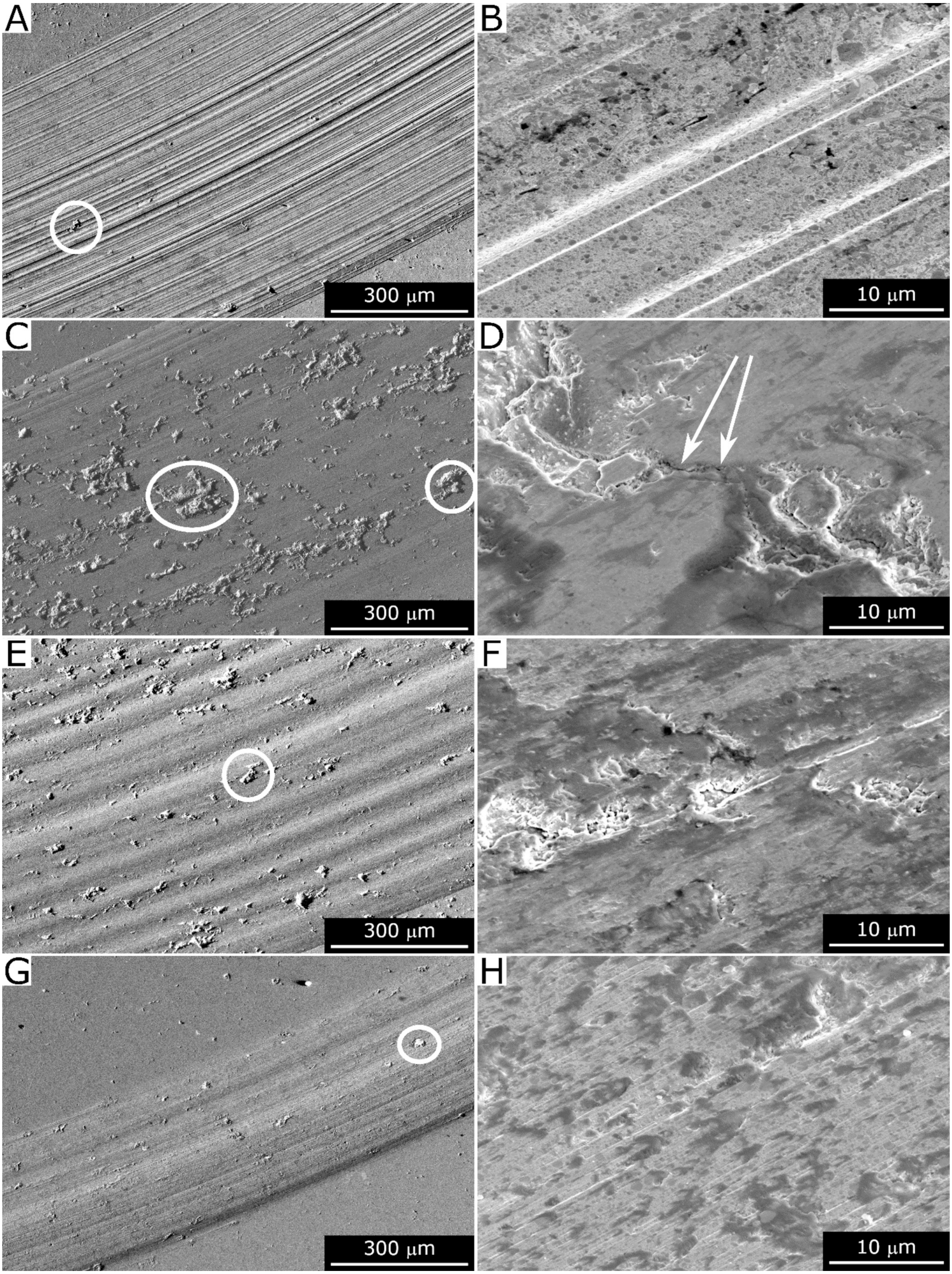

Fig. 15. SEM micrographs of ball-disc wear tracks produced on samples Cantor+60TiC Run3 (A, B), Al_0(CrMnFeNi) + 60TiC Run1 (C, D), Al_{14}(CrMnFeNi) + 60TiC Run3 (E, F), and AlCuCrFeNi+60TiC Run3 (G, H). Overviews (A, C, E, G) and magnified views (B, D, F, H). Circles indicate micropits; arrows in panel D indicate a crack.

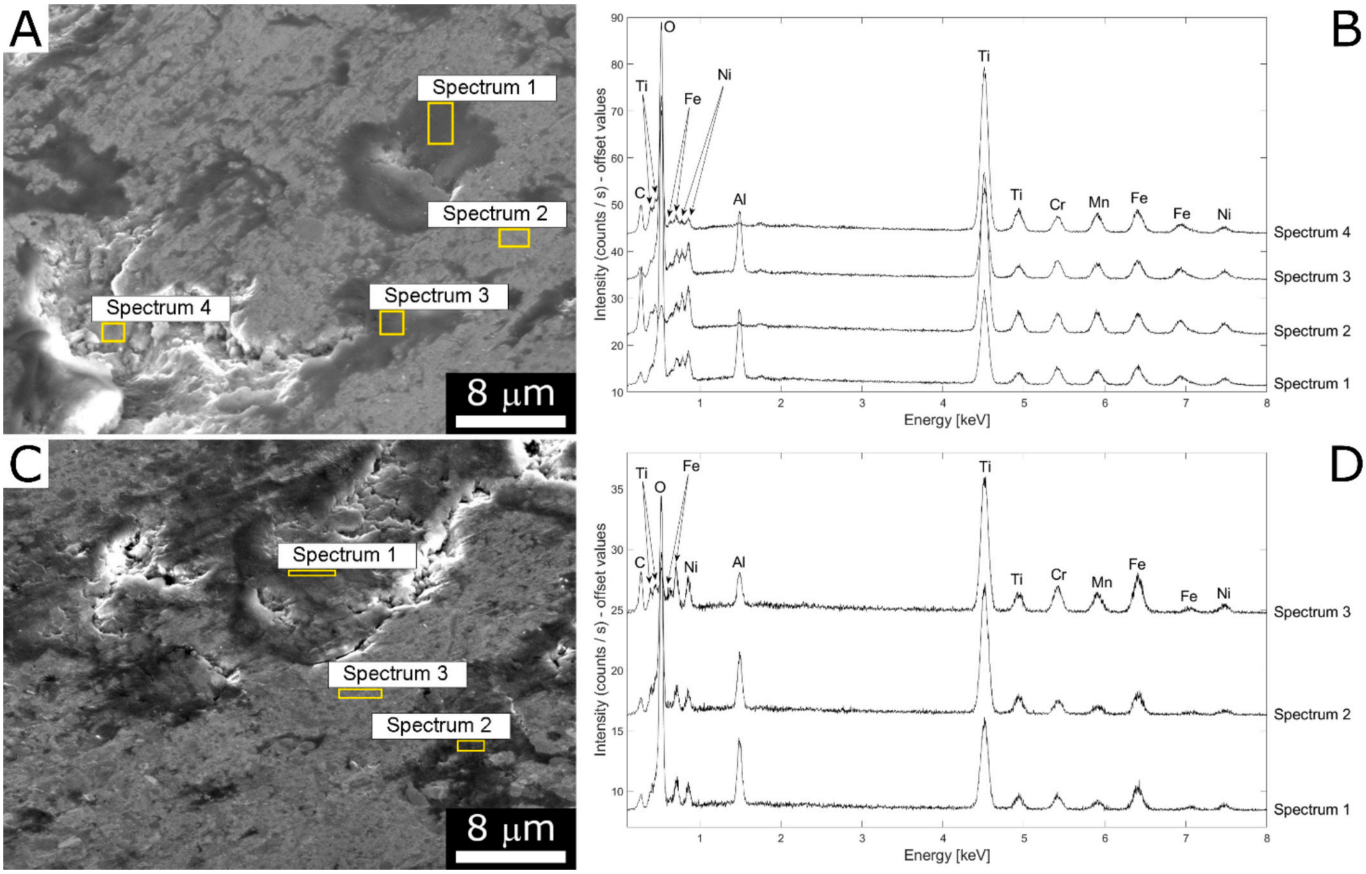

Fig. 16. SEM micrographs of the worn surfaces of the Cantor+60TiC Run 2 (A) and Al_{14}(CrMnFeNi) + 60TiC Run3 (C) samples after the ball-on-disc test, with the corresponding EDX spectra (B, D).

tougher Cantor+60TiC (Fig. 15A, B) and AlCuCrFeNi+60TiC (Fig. 15G, H) samples exhibited very few micropits, even under these particularly severe contact conditions characterized by a high initial hertzian contact pressure. In this case, abrasive grooves appeared, which could have been due to the hardness of these samples (<1000 HV, Section 3.3) being lower than is reported for other hardmetal coatings.

Furthermore, some tribo-oxidation also occurred, as revealed by the presence of some oxide clusters on the worn surfaces, mostly retained within the pits (Fig. 16A, B: spectra1, 3, 4; Fig. 16C, D: spectra 1, 2). The composition of these tribologically induced oxides differed from that of the oxide inclusions seen in Fig. 8. The inclusions were enriched in Ti; by contrast, in the tribologically induced oxides, the proportion of the various elements was closer to the initial composition of the hardmetal. The Raman spectra of the tribo-oxidized clusters (Fig. 17) also differed from those of the oxide inclusions (Fig. 9). The main constituent of the clusters was a spinel-type mixed oxide; titanium sub-oxides and/or ilmenite-type oxides, which were the main constituents of the inclusions, were minor constituents of the tribo-oxidized clusters. Therefore, the clusters might have been formed by a low-speed tribo-oxidation process [74] involving the debris released by the hardmetal surface. All the constituents of the alloy were oxidized when the very fine debris particles interacted with oxygen because of their high surface/volume ratio. This differed from the preferential reaction of only the most oxidizable element (Ti), which happened in a spontaneous, high-temperature-induced oxidation process. The content of Al in the tribo-oxidized clusters was a bit higher than in the base alloy (Fig. 16) because of the embedment of debris from the Al_2O_3 ball; however, Al never became the main constituent, since the specific wear rate of the balls was always lower than that of the corresponding flat samples.

On the other hand, the dry particle abrasion test elicited a combination of ductile grooving and brittle fracture in all samples (Fig. 18A, C, E). The abrasive particles, driven by the rotating wheel in a high-stress abrasion [19] configuration, caused indentation, ploughing and wedging/chipping on the coating. The high-magnification cross-sectional micrographs in Fig. 19B, D, and F specifically showed partially fragmented Al_2O_3 particles penetrating the sample surface and chipping out the coating material. The failure did not extend below the contact surface, as the overviews in Fig. 19A, C, and E did not show any crack deep into the coating.

It is difficult to identify qualitative differences among the worn surface morphologies of the various samples; however, Fig. 18D suggests that direct brittle fracture was more frequent in the more brittle samples (see the circled area). The tougher coatings, on the contrary, exhibited more frequently a ductile form of failure: the material underwent repeated plastic deformation and eventually delaminated (Fig. 18B and F: see arrows) due to low-cycle fatigue.

Compared to reference data acquired in this work and taken from our previous reports, the specific wear rates of the Cantor+60TiC and AlCuCrFeNi+60TiC coatings in the sliding wear tests (Fig. 13) were intermediate between those of HVOF-sprayed WC-CoCr and Cr_3C_2-NiCr coatings. Notably, the specific wear rate obtained for the WC-CoCr coating in this work was only slightly higher than the value reported in [45] for a similar coating tested using a 6 mm diameter sphere, which produced lower initial contact pressures. On the other hand, the wear rates of the Al_0(CrMnFeNi) + 60TiC samples were close to those of Cr_3C_2-NiCr, and the wear rates of the Al_{14}(CrMnFeNi) + 60TiC samples even exceeded those values. Moreover, all of the present samples were less sliding wear-resistant than HVOF-sprayed (Ti,Mo)(C,N)-Ni [57]. Thus, in terms of sliding wear resistance, these results show that more work is still needed on the compositional design of the HEA matrices to

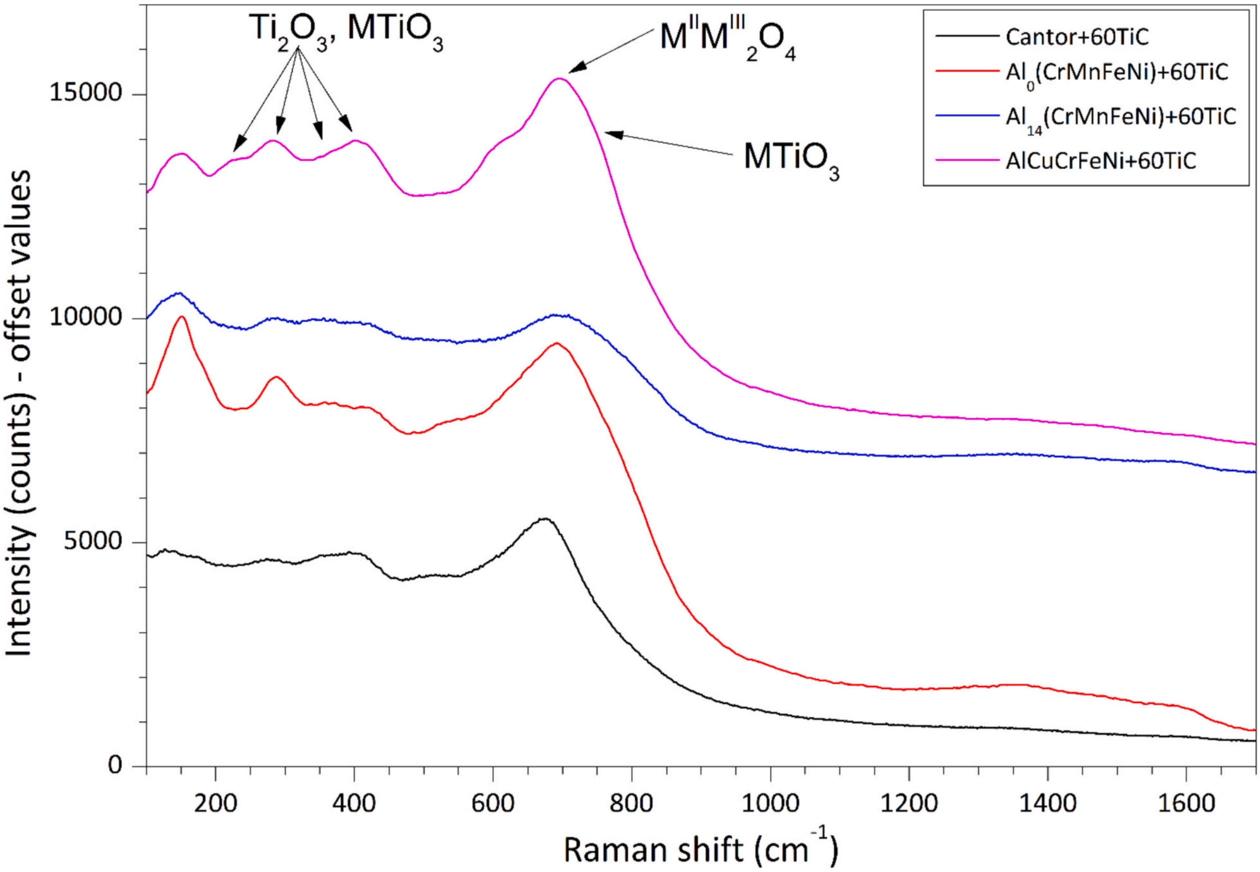

Fig. 17. Representative micro-Raman spectra acquired on oxide clusters found on the ball-on-disc sliding wear tracks of samples Cantor+60TiC Run 2, Al$_0$(CrMnFeNi) + 60TiC Run1, Al$_{14}$(CrMnFeNi) + 60TiC Run1, and AlCuCrFeNi+60TiC.

find the best balance between toughness (to prevent surface fatigue) and hardness (to limit abrasive grooving).

On the other hand, in the high-stress abrasion test (Fig. 14), the specific wear rates of the Cantor+60TiC and, in particular, the AlCuCrFeNi+60TiC coatings were almost on par with the value measured in [46] for HVOF-sprayed Cr_3C_2-NiCr, and much better than (Ti,Mo)(C,N)-Ni. The specific wear rate measured for HVOF-sprayed WC-CoCr in this work was also indistinguishable (within the error range) from the value previously obtained. The similarity between the specific wear rates of the AlCuCrFeNi+60TiC and Cr_3C_2-NiCr coatings is particularly noteworthy. In all our previous experiments with TiC-based hardmetal coatings that had simpler, Ni- or Fe-based matrices [19,44,45,57], the steel-wheel test had always returned poorer performances compared to Cr_3C_2-NiCr due to the brittleness of those coatings. It can be concluded that AlCuCrFeNi+60TiC coatings, with their comparatively low oxide content and a ductile HEA-based FCC metal matrix, provided a considerable advantage in this respect. Developments that aim to couple this toughness with slightly improved hardness (as mentioned previously) could clearly yield further benefits in this case as well. Specifically, the design of FCC matrices characterized by twinning or transformation-induced plasticity (TWIP or TRIP) might be a promising avenue to achieve the desired balance [9,42].

4. Conclusions

In the present work, hardmetal coatings consisting of a TiC hard phase in high-entropy alloy (HEA) matrices were obtained by HVOF spraying using feedstock powders produced by high-energy ball milling (HEBM). Matrix compositions were selected to cover a wide range of possibilities afforded by the vast compositional space of HEAs, going from cobalt-containing to cobalt-free formulations, from primarily BCC to mainly or fully FCC structures, and from Fe-rich to Ni-rich compositions.

The characterization of the microstructure, mechanical properties, and tribological behaviour of these coatings leads to the following conclusions:

- The materials could be sprayed with a reasonably high efficiency of up to 60 % through the HVOF process, and all coatings exhibited <1 vol% porosity.
- Ti-rich oxide inclusions existed in all coatings. The matrix composition had some effect on the degree of oxidation: coatings with the AlCuCrFeNi matrix were less oxidized compared to the others. The phase structure of the oxide inclusions also changed from predominantly ilmenite-type $MTiO_3$ and/or Ti_2O_3 in Al-free coatings to mostly cubic MO-type oxides with Al-containing matrices.
- Most of the fine, sub-micrometric, and nanometric TiC particles produced by HEBM were retained after HVOF deposition. However, the overall content of TiC obtained by Rietveld refinement of the XRD patterns decreased somewhat and a decarburized TiC_{1-x} phase with a hexagonal structure also appeared. The presence of Al in the matrix seemed beneficial in reducing the extent of decarburization, although the mechanisms by which this occurred are currently not fully understood.
- The HEBM process induced the formation of a BCC phase even in matrices that should exhibit solely an FCC structure. HVOF spraying brought the phase composition closer to that expected under thermodynamic equilibrium at solidus, with an excess of FCC phase instead.
- The hardness of the coatings was in the range of 750 to 900 HV_{3N}. While this large-scale test did not differentiate much among the samples, high-speed nanoindentation mapping revealed the

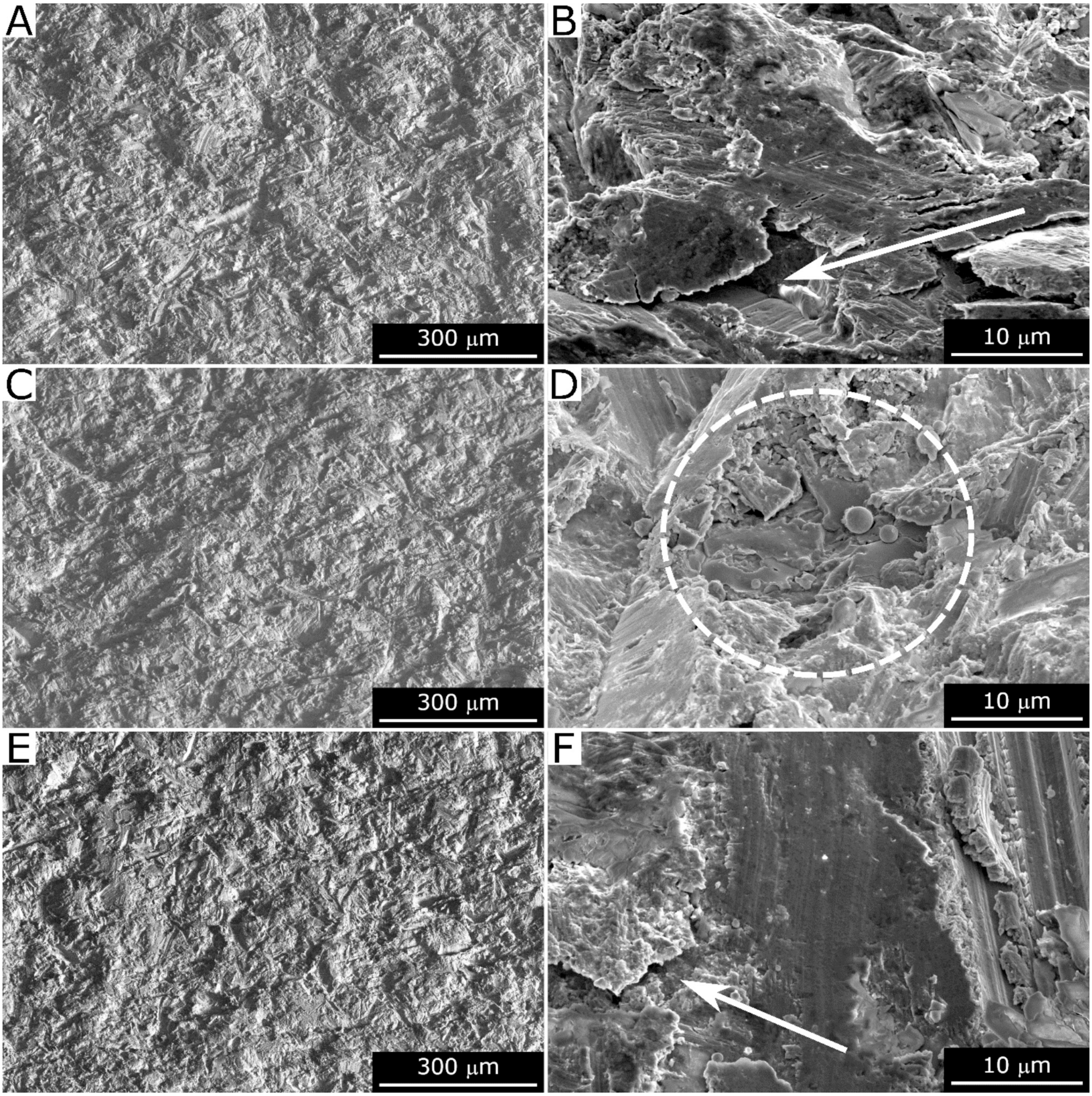

Fig. 18. SEM micrographs of the surfaces of the abrasion tracks produced on samples Cantor+60TiC Run2 (A, B), Al_{14}(CrMnFeNi) + 60TiC Run1 (C, D), and AlCuCrFeNi+60TiC Run2 (E, F). Overviews (A, C, E) and magnified views (B, D, F). The circle in panel D indicates a brittle fracture area; arrows in panels B and F indicate delamination of plastically fatigued areas.

differences between the hardness values of the softer FCC (~6–7 GPa) and the harder BCC (~12 GPa) phases in the matrices. These values are higher than those for bulk FCC and BCC HEAs, presumably because of the extremely fine-grained structure of a HVOF coating, the dissolution of some Ti and C during spraying, and the possible influence of the finely dispersed nanometric TiC particles on the measurement. The TiC phase, on the other hand, had the expected high hardness of ~22 GPa.

- Other differences emerged in terms of toughness, as revealed by scratch tests with linearly increasing loads. Chipping of the coating surface along the scratch groove began at a lower critical load with the Al_0(CrMnFeNi)-60TiC and Al_{14}(CrMnFeNi) + 60TiC compositions compared to the Cantor+60TiC and AlCuCrFeNi+60TiC ones. This can be associated with the presence of a substantial amount of BCC phase (harder but also, likely, more brittle) in the Al_{14}(CrMnFeNi) matrix and with Fe as the main constituent of the Al_0(CrMnFeNi) and Al_{14}(CrMnFeNi) alloys. Previous experiences with simpler (non-HEA) compositions also suggested that hardmetal coatings with Fe-rich matrices were more brittle than those with Ni-based matrices.
- The main sliding wear mechanism of the Al_0(CrMnFeNi) + 60TiC and Al_{14}(CrMnFeNi) + 60TiC coatings in the ball-on-disc test against a hard counterbody (Al_2O_3) was surface fatigue in the form of micropitting. The brittleness of the material facilitated the propagation of fatigue microcracks. On the contrary, the Cantor+60TiC and AlCuCrFeNi+60TiC compositions mainly exhibited two-body ductile grooving, with lower specific wear rates of ~1.5–2 × 10^{-6} $mm^3/(N \cdot m)$.

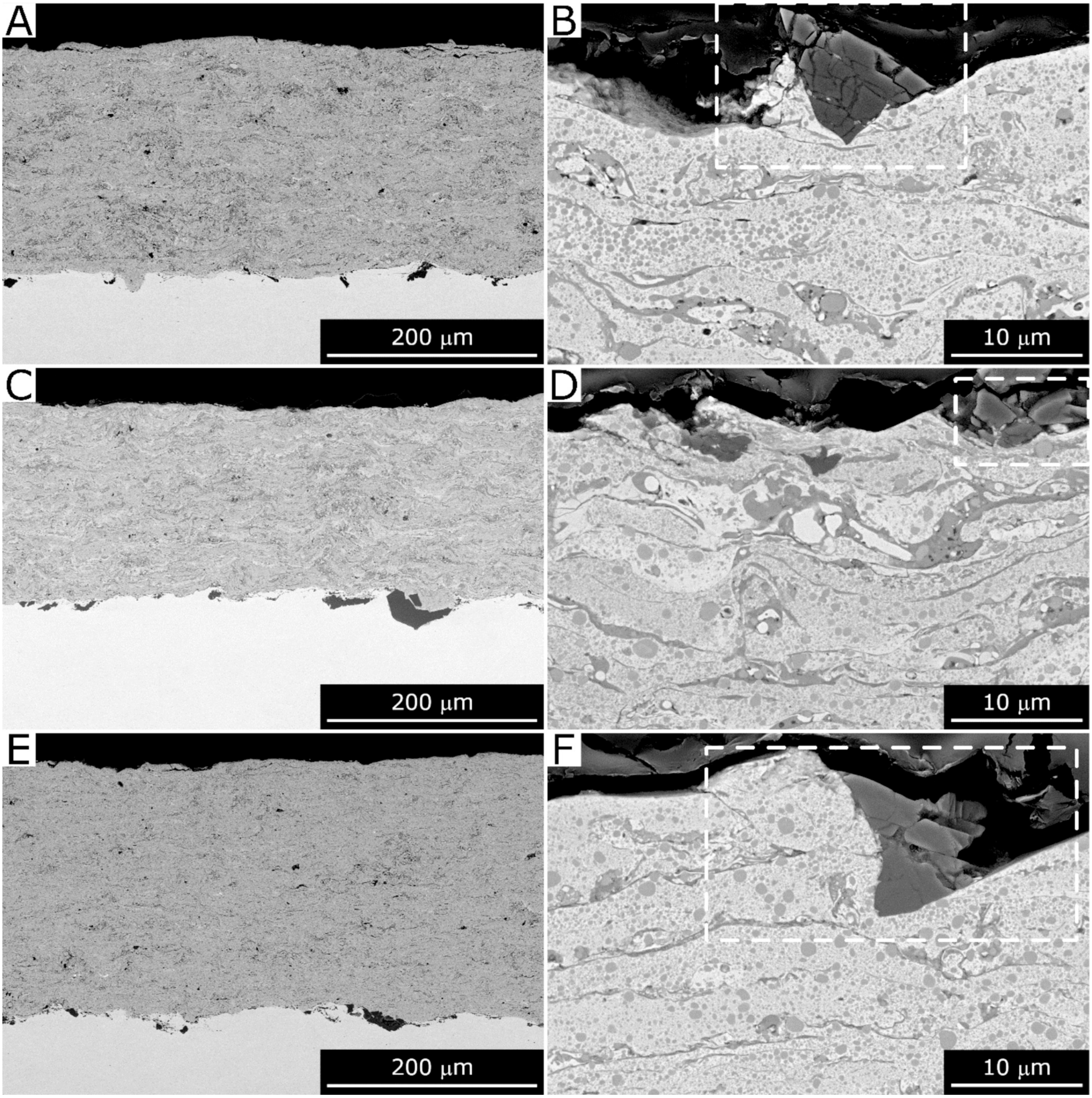

Fig. 19. Backscattered electron SEM micrographs of the cross-sections of the abrasion tracks produced on samples Cantor+60TiC Run2 (A, B), Al_{14}(CrMnFeNi) + 60TiC Run1 (C, D), and AlCuCrFeNi+60TiC Run2 (E, F). Overviews (A, C, E) and magnified views (B, D, F). Dashed rectangles in panels B, D, F show embedded fragments of abrasive particles the indent and chip the coatings.

- In a high-stress abrasion test, the Al_0(CrMnFeNi) + 60TiC and Al_{14}(CrMnFeNi) + 60TiC coatings also exhibited more severe wear associated with a higher incidence of brittle fracture. The AlCuCrFeNi+60TiC composition, with its low oxide content, exhibited a specific wear rate of 1.2–1.5 × 10^{-3} mm^3/(N·m), comparable to the value reported for Cr_3C_2-25wt.%NiCr under the same conditions. Its wear mechanisms included a higher incidence of ductile grooving and particles' indentation.
- In any case, the HVOF deposition of these materials was shown to be quite robust with respect to the process parameters: a change from "low" to "medium" and "high" gas flow rate settings did not produce measurable differences in any of the tests performed in this work.

Overall, the methodology and approaches used in this work were effective in producing wear and corrosion-resistant coatings. Although not yet fully competitive with the existing solutions, these HEA-TiC systems set the basis for a material dataset that will enable numerical models to guide the development of new and more performing solutions.

CRediT authorship contribution statement

Giovanni Bolelli: Visualization, Supervision, Project administration, Methodology, Investigation, Funding acquisition, Formal analysis, Data curation, Writing – original draft. **Maria Francesca Bonilauri:** Investigation, Formal analysis, Writing – review & editing. **Luca**

Bortolotti: Investigation, Formal analysis, Writing – review & editing. **Alessia Bruera:** Investigation. **Margherita Cescon:** Investigation. **Lorenzo Ferrari:** Investigation, Formal analysis. **Magdalena Lassinantti Gualtieri:** Investigation, Formal analysis, Writing – review & editing. **Luca Lusvarghi:** Supervision, Funding acquisition, Conceptualization, Writing – review & editing. **Stefania Morelli:** Investigation, Formal analysis, Writing – review & editing. **Milena Pazzi:** Investigation. **Alvise Bianchin:** Supervision, Project administration, Methodology, Investigation, Funding acquisition, Conceptualization, Writing – review & editing. **Enrico Forlin:** Methodology, Investigation, Conceptualization, Writing – review & editing. **Giulia Gigante:** Investigation, Formal analysis, Writing – review & editing. **Edoardo Rossi:** Investigation, Formal analysis, Writing – review & editing. **Marco Sebastiani:** Supervision, Investigation, Formal analysis, Writing – review & editing.

Declaration of competing interest

The authors declare the following financial interests/personal relationships which may be considered as potential competing interests: All authors report financial support was provided by European Union under GA no 101092211. Alvise Bianchin, Enrico Forlin report a relationship with MBN Nanomaterialia Srl that includes: employment. If there are other authors, they declare that they have no known competing financial interests or personal relationships that could have appeared to influence the work reported in this paper.

Data availability

The data is part of an ongoing project and will be made available at a later stage.

Acknowledgements

This work was Funded by the European Union under GA no 101092211; Project name: “Integrated Computational-Experimental material Engineering of Thermal Spray coatings”; Project acronym: “CoBRAIN”; call topic: HORIZON-CL4-2022-RESILIENCE-01-19; Granting authority: European Health and Digital Executive Agency (HADEA). Views and opinions expressed are, however, those of the author(s) only and do not necessarily reflect those of the European Union or HADEA. Neither the European Union nor the granting authority can be held responsible for them.

The authors would like to thank Dr. Miriam Hanuskova (University of Modena and Reggio Emilia, Modena, Italy) for performing the particle size distribution analyses on the feedstock powders.

References

[1] Z. Li, S. Zhao, R.O. Ritchie, M.A. Meyers, Mechanical properties of high-entropy alloys with emphasis on face-centered cubic alloys, Prog. Mater. Sci. 102 (2019) 296–345, https://doi.org/10.1016/j.pmatsci.2018.12.003.

[2] D.B. Miracle, O.N. Senkov, A critical review of high entropy alloys and related concepts, Acta Mater. 122 (2017) 448–511, https://doi.org/10.1016/j.actamat.2016.08.081.

[3] O.N. Senkov, J.D. Miller, D.B. Miracle, C. Woodward, Accelerated exploration of multi-principal element alloys for structural applications, CALPHAD 50 (2015) 32–48, https://doi.org/10.1016/j.calphad.2015.04.009.

[4] F. Tancret, I. Toda-Caraballo, E. Menou, P.E.J. Rivera Díaz-Del-Castillo, Designing high entropy alloys employing thermodynamics and Gaussian process statistical analysis, Mater. Des. 115 (2017) 486–497, https://doi.org/10.1016/j.matdes.2016.11.049.

[5] S. Guo, C. Ng, J. Lu, C.T. Liu, Effect of valence electron concentration on stability of fcc or bcc phase in high entropy alloys, J. Appl. Phys. 109 (2011) 103505, https://doi.org/10.1063/1.3587228.

[6] Y. Zhang, T.T. Zuo, Z. Tang, M.C. Gao, K.A. Dahmen, P.K. Liaw, Z.P. Lu, Microstructures and properties of high-entropy alloys, Prog. Mater. Sci. 61 (2014) 1–93, https://doi.org/10.1016/j.pmatsci.2013.10.001.

[7] B. Cantor, Multicomponent high-entropy Cantor alloys, Prog. Mater. Sci. 120 (2021) 100754, https://doi.org/10.1016/j.pmatsci.2020.100754.

[8] B. Gludovatz, A. Hohenwarter, D. Catoor, E.H. Chang, E.P. George, R.O. Ritchie, A fracture-resistant high-entropy alloy for cryogenic applications, Science 345 (2014) 1153–1158, https://doi.org/10.1126/science.1254581.

[9] H.Y. Diao, R. Feng, K.A. Dahmen, P.K. Liaw, Fundamental deformation behavior in high-entropy alloys: an overview, Curr. Opin. Solid State Mater. Sci. 21 (2017) 252–266, https://doi.org/10.1016/j.cossms.2017.08.003.

[10] K.N. Yoon, H.S. Oh, J.Y. Kim, M.S. Kim, J. Zhang, E.S. Park, A new class of light-weight metastable high entropy alloy with high strength and large ductility, Materialia 21 (2022) 101284, https://doi.org/10.1016/j.mtla.2021.101284.

[11] Z. Zeng, M. Xiang, D. Zhang, J. Shi, W. Wang, X. Tang, W. Tang, Y. Wang, X. Ma, Z. Chen, W. Ma, K. Morita, Mechanical properties of Cantor alloys driven by additional elements: a review, J. Mater. Res. Technol. 15 (2021) 1920–1934, https://doi.org/10.1016/J.JMRT.2021.09.019.

[12] A. Ayyagari, V. Hasannaeimi, H.S. Grewal, H. Arora, S. Mukherjee, Corrosion, erosion and wear behavior of complex concentrated alloys: a review, Metals 8 (2018) 603, https://doi.org/10.3390/met8080603.

[13] A. Kumar, A. Singh, A. Suhane, Mechanically alloyed high entropy alloys: existing challenges and opportunities, J. Mater. Res. Technol. 17 (2022) 2431–2456, https://doi.org/10.1016/j.jmrt.2022.01.141.

[14] J. Liu, H. Yu, C. Chen, F. Weng, J. Dai, Research and development status of laser cladding on magnesium alloys: a review, Opt. Lasers Eng. 93 (2017) 195–210, https://doi.org/10.1016/j.optlaseng.2017.02.007.

[15] A. Meghwal, A. Anupam, B.S. Murty, C.C. Berndt, R.S. Kottada, A.S.M. Ang, Thermal spray high-entropy alloy coatings: a review, J. Therm. Spray Technol. 29 (2020) 857–893, https://doi.org/10.1007/s11666-020-01047-0.

[16] X.H. Yan, J.S. Li, W.R. Zhang, Y. Zhang, A brief review of high-entropy films, Mater. Chem. Phys. 210 (2018) 12–19, https://doi.org/10.1016/j.matchemphys.2017.07.078.

[17] P. Kulu, I. Kleis, Erosion resistance of powder materials and coatings, in: Solid Particle Erosion, Springer London, London, UK, 2008, pp. 129–168, https://doi.org/10.1007/978-1-84800-029-2_4.

[18] M. Xiao, S. Nai, S. Nan, C. Feng, Z. Guan, C. Huo, F. Zhang, Z. Qiu, G. Li, Preparation, mechanical properties and wear resistance of dual-sized TiC particles reinforced high-entropy alloy cermet coating, J. Mater. Res. Technol. 28 (2024) 97–109, https://doi.org/10.1016/j.jmrt.2023.11.264.

[19] V. Testa, S. Morelli, G. Bolelli, F. Bosi, P. Puddu, A. Colella, T. Manfredini, L. Lusvarghi, Corrosion and wear performances of alternative TiC-based thermal spray coatings, Surf. Coat. Technol. 438 (2022) 128400, https://doi.org/10.1016/j.surfcoat.2022.128400.

[20] J. Lv, Y. Wu, S. Hong, J. Cheng, Y. Chen, J. Cheng, Z. Wei, S. Zhu, Effects of WC addition on the erosion behavior of high-velocity oxygen fuel sprayed AlCoCrFeNi high-entropy alloy coatings, Ceram. Int. 48 (2022) 18502–18512, https://doi.org/10.1016/j.ceramint.2022.03.120.

[21] S. Li, W. Niu, Y.-W. Lei, Y. Zheng, Microstructure and wear performance of ex/in-situ TiC reinforced CoCrFeNiW0.4Si0.2 high-entropy alloy coatings by laser cladding, J. Alloys Compd. 1002 (2024) 175458, https://doi.org/10.1016/j.jallcom.2024.175458.

[22] L. Chen, Y. Lan, Y. Cheng, J. Zeng, Y. Ma, S. Yu, Z. Ding, B. Liu, J. Zhang, H. Peng, W. Guo, Friction behavior and wear mechanism of laser cladded FeNiCr-WC composite coatings in comparison with different friction pairs, J. Mater. Res. Technol. 31 (2024) 1956–1973, https://doi.org/10.1016/j.jmrt.2024.06.206.

[23] H. Liang, J. Hou, X. Li, L. Jiang, Z. Cao, Micro-structures and dry sliding wear properties of novel AlCrFeNiMo0.5-x(WC) high entropy alloy-ceramic composite coatings, Intermetallics 170 (2024) 108328, https://doi.org/10.1016/j.intermet.2024.108328.

[24] Z. Wang, G. Wang, Z. Song, S. Liu, Y. Zhou, X. Qiu, C. Wu, X. Wang, Z. Chen, C. Meng, Microstructure evolution, wear and corrosion behavior of WC reinforced CoCrFeNiMn high-entropy alloy composite coatings by induction cladding, Surf. Coat. Technol. 486 (2024) 130938, https://doi.org/10.1016/j.surfcoat.2024.130938.

[25] H. Liu, R. Wang, J. Hao, X. Liu, P. Chen, H. Yang, T. Zhang, Microstructural evolution and wear characteristics of laser-clad CoCrFeNiMn high-entropy alloy coatings incorporating tungsten carbide, J. Alloys Compd. 976 (2024) 173124, https://doi.org/10.1016/j.jallcom.2023.173124.

[26] J. Wang, J. Man, Q. Wang, G. Liu, S. Xiao, N. Dong, Effect of nano WC on wear and corrosion resistances of CoCrFeNiTi high entropy alloy coating, J. Mater. Eng. Perform. (2024), https://doi.org/10.1007/s11665-023-09125-4.

[27] B. Chen, G. Zhang, Z. Zhang, X. Wang, L. Gao, X. Song, Effect of niobium content on microstructure and wear and corrosion resistance of laser-clad FeCo0.5CrNi1.5B0.5Nbx coatings on ductile iron, Surf. Coat. Technol. 476 (2024) 130210, https://doi.org/10.1016/j.surfcoat.2023.130210.

[28] G.A. Blengini, C. EL Latunussa, U. Eynard, C. Torres de Matos, D. Wittmer, K. Georgitzikis, C. Pavel, S. Carrara, L. Mancini, M. Unguru, D. Blagoeva, F. Mathieux, D. Pennington, Study on the EU’s List of Critical Raw Materials – Final Report, Brussels, Belgium, 2020, https://doi.org/10.2873/11619.

[29] D.G. Barceloux, D. Barceloux, Cobalt, J. Toxicol. Clin. Toxicol. 37 (1999) 201–216, https://doi.org/10.1081/CLT-100102420.

[30] Industry Actions for Responsible Assessment and Classification of Cobalt Compounds, The Cobalt Development Institute. www.cobaltreachconsortium.org/web_images//documents/One-page-statement-Industry-Actions.pdf, 2013. (Accessed 5 July 2015).

[31] D. Lison, S. van den Brule, G. Van Maele-Fabry, Cobalt and its compounds: update on genotoxic and carcinogenic activities, Crit. Rev. Toxicol. 48 (2018) 522–539, https://doi.org/10.1080/10408444.2018.1491023.

[32] NTP - U.S. Department of Health and Human Services, Toxicology Studies of Cobalt Metal (CAS No. 7440-48-4) in F344/N Rats and B6C3F1/N Mice and Toxicology

and Carcinogenesis Studies of Cobalt Metal (CAS No. 7440-48-4) in F344/N Rats and B6C3F1/N Mice (Inhalation Studies). https://www.ncbi.nlm.nih.gov/books/NBK567171/, 2014. (Accessed 1 September 2024).

[33] CLH report: Proposal for Harmonised Classification and Labelling Based on Regulation (EC) No 1272/2008 (CLP Regulation), Annex VI, Part 2. Substance Name: Cobalt. https://echa.europa.eu/documents/10162/d1ca0305-88d5-5b07-69ee-1f4312c1951f, 2019. (Accessed 22 March 2019) (1–157).

[34] T. Santonen, V.M. Varnai, Committee for Risk Assessment RAC Opinion proposing harmonised classification and labelling at EU level of cobalt - EC Number: 231-158-0 CAS Number: 7440-48-4, Helsinki. https://echa.europa.eu/documents/10162/b7316b11-ae65-1dd0-2e64-bb6ad3efbd82, 2017. (Accessed 3 September 2024).

[35] D. Lee, Wear-resistant coatings, in: R.C. Tucker Jr. (Ed.), ASM Handbook - Volume 5A: Thermal Spray Technology, ASM International, Materials Park, OH, USA, OH, USA, 2013, pp. 253–256, https://doi.org/10.31399/asm.hb.v05a.a0005734.

[36] M.R. Dorfman, Corrosion and wear control for industrial applications, in: R. C. Tucker Jr. (Ed.), ASM Handbook - Volume 5A: Thermal Spray Technology, ASM International, Materials Park, OH, USA, 2013, pp. 257–261, https://doi.org/10.31399/asm.hb.v05a.a0005735.

[37] S. Matthews, B. James, Review of thermal spray coating applications in the steel industry: part 2 - zinc pot hardware in the continuous galvanizing line, J. Therm. Spray Technol. 19 (2010) 1277–1286, https://doi.org/10.1007/s11666-010-9519-7.

[38] S. Matthews, B. James, Review of thermal spray coating applications in the steel industry: part 1 - hardware in steel making to the continuous annealing process, J. Therm. Spray Technol. 19 (2010) 1267–1276, https://doi.org/10.1007/s11666-010-9518-8.

[39] M. Pollack, Replacement for hard chrome plating on aircraft landing gear, in: R. C. Tucker Jr. (Ed.), ASM Handbook - Volume 5A: Thermal Spray Technology, ASM International, Materials Park, OH, USA, 2013, pp. 296–297, https://doi.org/10.31399/asm.hb.v05a.a0005739.

[40] M.R. Dorfman, A. Sharma, Thermal spray applications in the paper production industry, in: R.C. Tucker Jr. (Ed.), ASM handbook - Volume 5A: Thermal Spray Technology, ASM International, Materials Park, OH, USA, 2013, pp. 328–331, https://doi.org/10.31399/asm.hb.v05a.a0005743.

[41] N.D. Stepanov, D.G. Shaysultanov, R.S. Chernichenko, M.A. Tikhonovsky, S. V. Zherebtsov, Effect of Al on structure and mechanical properties of Fe-Mn-Cr-Ni-Al non-equiatomic high entropy alloys with high Fe content, J. Alloys Compd. 770 (2019) 194–203, https://doi.org/10.1016/j.jallcom.2018.08.093.

[42] Y.F. Ye, Q. Wang, J. Lu, C.T. Liu, Y. Yang, High-entropy alloy: challenges and prospects, Mater. Today 19 (2016) 349–362, https://doi.org/10.1016/j.mattod.2015.11.026.

[43] C. Ng, S. Guo, J. Luan, Q. Wang, J. Lu, S. Shi, C.T. Liu, Phase stability and tensile properties of Co-free Al 0.5CrCuFeNi2 high-entropy alloys, J. Alloys Compd. 584 (2014) 530–537, https://doi.org/10.1016/j.jallcom.2013.09.105.

[44] G. Bolelli, A. Colella, L. Lusvarghi, P. Puddu, R. Rigon, P. Sassatelli, V. Testa, Properties of HVOF-sprayed TiC-FeCrAl coatings, Wear 418 (2019) 36–51, https://doi.org/10.1016/j.wear.2018.11.002.

[45] G. Bolelli, A. Colella, L. Lusvarghi, S. Morelli, P. Puddu, E. Righetti, P. Sassatelli, V. Testa, TiC–NiCr thermal spray coatings as an alternative to WC-CoCr and Cr_3C_2–NiCr, Wear 450–451 (2020) 203273, https://doi.org/10.1016/j.wear.2020.203273.

[46] L. Rossi Gehlen, G. Bolelli, P. Puddu, E. Forlin, A. Colella, G. Pintaude, L. Lusvarghi, Tribological and electrochemical performances of HVOF sprayed NbC-NiCr coatings, Surf. Coat. Technol. 474 (2023) 130098, https://doi.org/10.1016/j.surfcoat.2023.130098.

[47] G. Bolelli, M.F. Bonilauri, P. Sassatelli, F. Bruno, R. Franci, G. Pulci, F. Marra, L. Paglia, G.C. Gazzadi, S. Frabboni, L. Lusvarghi, Pre-treatment of Selective Laser Melting (SLM) surfaces for thermal spray coating, Surf. Coat. Technol. 441 (2022) 128533, https://doi.org/10.1016/j.surfcoat.2022.128533.

[48] T. Degen, M. Sadki, E. Bron, U. König, G. Nénert, The HighScore suite, Powder Diffract. 29 (2014) S13–S18, https://doi.org/10.1017/S0885715614000840.

[49] A.C. Larson, R.B. Von Dreele, General Structure Analysis System (GSAS), Los Alamos, 1994.

[50] B.H. Toby, EXPGUI, a graphical user interface for GSAS, J. Appl. Crystallogr. 34 (2001) 210–213, https://doi.org/10.1107/S0021889801002242.

[51] S. Gražulis, A. Daškevič, A. Merkys, D. Chateigner, L. Lutterotti, M. Quirós, N. R. Serebryanaya, P. Moeck, R.T. Downs, A. Le Bail, Crystallography Open Database (COD): an open-access collection of crystal structures and platform for world-wide collaboration, Nucleic Acids Res. 40 (2012) D420–D427, https://doi.org/10.1093/NAR/GKR900.

[52] E. Rossi, J.M.J.M. Wheeler, M. Sebastiani, High-speed nanoindentation mapping: a review of recent advances and applications, Curr. Opin. Solid State Mater. Sci. 27 (2023) 101107, https://doi.org/10.1016/j.cossms.2023.101107.

[53] W.C. Oliver, G.M. Pharr, An improved technique for determining hardness and elastic modulus using load and displacement sensing indentation experiments, J. Mater. Res. 7 (1992) 1564–1583, https://doi.org/10.1557/jmr.1992.1564.

[54] H. Besharatloo, J.M. Wheeler, Influence of indentation size and spacing on statistical phase analysis via high-speed nanoindentation mapping of metal alloys, J. Mater. Res. 36 (2021) 2198–2212, https://doi.org/10.1557/s43578-021-00214-5.

[55] P. Sudharshan Phani, W.C. Oliver, A critical assessment of the effect of indentation spacing on the measurement of hardness and modulus using instrumented indentation testing, Mater. Des. 164 (2019) 107563, https://doi.org/10.1016/j.matdes.2018.107563.

[56] S. Chander, P. Vijaya, Unsupervised Learning Methods for Data Clustering, Artificial Intelligence in Data Mining: Theories and Applications, 2021, pp. 41–64, https://doi.org/10.1016/B978-0-12-820601-0.00002-1.

[57] G. Bolelli, C. Lyphout, L.M. Berger, V. Testa, H. Myalska-Głowacka, P. Puddu, P. Sassatelli, L. Lusvarghi, Wear resistance of HVOF- and HVAF-sprayed (Ti,Mo)(C,N)–Ni coatings from an agglomerated and sintered powder, Wear (2023) 204550, https://doi.org/10.1016/J.WEAR.2022.204550.

[58] S. Deshpande, S. Sampath, H. Zhang, Mechanisms of oxidation and its role in microstructural evolution of metallic thermal spray coatings - case study for Ni-Al, Surf. Coat. Technol. 200 (2006) 5395–5406, https://doi.org/10.1016/j.surfcoat.2005.07.072.

[59] C.M. Hackett, G.S. Settles, J.D. Miller, On the gas dynamics of HVOF thermal sprays, J. Therm. Spray Technol. 3 (1994) 299–304, https://doi.org/10.1007/BF02646278.

[60] R170055 - RRUFF Database: Raman, X-ray, Infrared, and Chemistry. https://rruff.info/chem=Ti,O/notchem=all/display=default/R170055. (Accessed 27 June 2024).

[61] W. Qi, A. Mattursun, M. Gao, A. Hushur, H. Zhang, Lattice dynamics of NiTiO3 under high pressure: Raman evidence under two pressure-transmitting mediums, Results Phys. 43 (2022) 106114, https://doi.org/10.1016/J.RINP.2022.106114.

[62] L.-M. Berger, Application of hardmetals as thermal spray coatings, Int. J. Refract. Met. Hard Mater. 49 (2015) 350–364, https://doi.org/10.1016/j.ijrmhm.2014.09.029.

[63] S. Matthews, B. James, M. Hyland, The role of microstructure in the mechanism of high velocity erosion of Cr_3C_2-NiCr thermal spray coatings: part 1 - As-sprayed coatings, Surf. Coat. Technol. 203 (2009) 1086–1093, https://doi.org/10.1016/j.surfcoat.2008.10.005.

[64] C.A. da Cunha, N.B. de Lima, J.R. Martinelli, A.H. de A. Bressiani, A.G.F. Padial, L. V. Ramanathan, Microstructure and mechanical properties of thermal sprayed nanostructured Cr_3C_2-Ni20Cr coatings, Mater. Res. 11 (2008) 137–143, https://doi.org/10.1590/S1516-14392008000200005.

[65] Q. Liu, Y. Bai, H.D. Wang, G.Z. Ma, M. Liu, C.Y. Chu, Y.W. Sun, W. Fan, F. Ding, B. Zhao, Y.T. Wang, Microstructural evolution of carbides and its effect on tribological properties of SAPS or HVOF sprayed NiCr–Cr_3C_2 coatings, J. Alloys Compd. 803 (2019) 730–741, https://doi.org/10.1016/j.jallcom.2019.06.291.

[66] J. Liu, T. Chen, C. Yuan, X. Bai, Performance analysis of cavitation erosion resistance and corrosion behavior of HVOF-sprayed WC-10Co-4Cr, WC-12Co, and Cr3C2-NiCr coatings, J. Therm. Spray Technol. 29 (2020) 798–810, https://doi.org/10.1007/s11666-020-00994-y.

[67] S. Hong, J. Qin, J. Lin, Y. Wu, J. Li, Y. Zheng, Influences of sand concentration and flow velocity on hydro-abrasive erosion behaviors of HVOF sprayed Cr_3C_2–NiCr and WC–Cr3C2–Ni coatings, J. Mater. Res. Technol. 21 (2022) 1507–1518, https://doi.org/10.1016/j.jmrt.2022.10.003.

[68] G. Bolelli, L.-M. Berger, T. Börner, H. Koivuluoto, L. Lusvarghi, C. Lyphout, N. Markocsan, V. Matikainen, P. Nylén, P. Sassatelli, R. Trache, P. Vuoristo, Tribology of HVOF- and HVAF-sprayed WC–10Co4Cr hardmetal coatings: a comparative assessment, Surf. Coat. Technol. 265 (2015) 125–144, https://doi.org/10.1016/j.surfcoat.2015.01.048.

[69] H. Warlimont, Ceramics, in: W. Martienssen, H. Warlimont (Eds.), Springer handbook of condensed matter and materials data, Springer Berlin Heidelberg, Berlin, Germany, 2005, pp. 431–476, https://doi.org/10.1007/3-540-30437-1_6.

[70] F. Cardarelli, Ceramics, refractories, and glasses, in: Materials Handbook, Springer, London, 2008, pp. 593–689, https://doi.org/10.1007/978-1-84628-669-8_10.

[71] S. Gorsse, M.H. Nguyen, O.N. Senkov, D.B. Miracle, Corrigendum to database on the mechanical properties of high entropy alloys and complex concentrated alloys, data in brief 21 (2018) 2664–2678, Data Brief 32 (2020) 106216, https://doi.org/10.1016/j.dib.2020.106216.

[72] W.D. Nix, H. Gao, Indentation size effects in crystalline materials: a law for strain gradient plasticity, J. Mech. Phys. Solids 46 (1998) 411–425, https://doi.org/10.1016/S0022-5096(97)00086-0.

[73] Z. Han, W. Ren, J. Yang, Y. Du, R. Wei, C. Zhang, Y. Chen, G. Zhang, The deformation behavior and strain rate sensitivity of ultra-fine grained CoNiFeCrMn high-entropy alloys at temperatures ranging from 77 K to 573 K, J. Alloys Compd. 791 (2019) 962–970, https://doi.org/10.1016/J.JALLCOM.2019.03.373.

[74] G. Straffelini, Wear mechanisms, in: Friction and Wear - Methodologies for Design and Control, Springer International Publishing AG, Cham, Switzerland, 2015, pp. 85–113, https://doi.org/10.1007/978-3-319-05894-8_4.